

WHO 2016 subtyping and automated segmentation of glioma using multi-task deep learning

Sebastian R. van der Voort^{1,†}, Fatih Incekara^{2,3,†}, Maarten MJ Wijnenga⁴, Georgios Kapsas², Renske Gahrman², Joost W Schouten³, Rishi Nandoe Tewarie⁵, Geert J Lycklama⁶, Philip C De Witt Hamer⁷, Roelant S Eijgelaar⁷, Pim J French⁴, Hendrikus J Dubbink⁸, Arnaud JPE Vincent³, Wiro J Niessen^{1,9}, Martin J van den Bent⁴, Marion Smits^{2,††}, and Stefan Klein^{1,††,*}

¹Biomedical Imaging Group Rotterdam, Department of Radiology and Nuclear Medicine, Erasmus MC University Medical Centre Rotterdam, Rotterdam, the Netherlands

²Department of Radiology and Nuclear Medicine, Erasmus MC University Medical Centre Rotterdam, Rotterdam, the Netherlands

³Department of Neurosurgery, Brain Tumor Center, Erasmus MC University Medical Centre Rotterdam, Rotterdam, the Netherlands

⁴Department of Neurology, Brain Tumor Center, Erasmus MC Cancer Institute, Rotterdam, the Netherlands

⁵Department of Neurosurgery, Haaglanden Medical Center, the Hague, the Netherlands

⁶Department of Radiology, Haaglanden Medical Center, the Hague, the Netherlands

⁸Department of Pathology, Brain Tumor Center at Erasmus MC Cancer Institute, Rotterdam, the Netherlands

⁹Imaging Physics, Faculty of Applied Sciences, Delft University of Technology, Delft, the Netherlands

⁷Department of Neurosurgery, Cancer Center Amsterdam, Brain Tumor Center, Amsterdam UMC, Amsterdam, Netherlands

[†]These authors contributed equally

^{††}These authors contributed equally

*Corresponding author; s.klein@erasmusmc.nl

Abstract

Accurate characterization of glioma is crucial for clinical decision making. A delineation of the tumor is also desirable in the initial decision stages but is a time-consuming task. Leveraging the latest GPU capabilities, we developed a single multi-task convolutional neural network that uses the full 3D, structural, pre-operative MRI scans to can predict the IDH mutation status, the 1p/19q co-deletion status, and the grade of a tumor, while simultaneously segmenting the tumor. We trained our method using the largest, most diverse patient cohort to date containing 1508 glioma patients from 16 institutes. We tested our method on an independent dataset of 240 patients from 13 different institutes, and achieved an IDH-AUC of 0.90, 1p/19q-AUC of 0.85, grade-AUC of 0.81, and a mean whole tumor DICE score of 0.84. Thus, our method non-invasively predicts multiple, clinically relevant parameters and generalizes well to the broader clinical population.

1 Introduction

Glioma is the most common primary brain tumor and is one of the deadliest forms of cancer [1]. Differences in survival and treatment response of glioma are attributed to their genetic and histological features, specifically the isocitrate dehydrogenase (IDH) mutation status, the 1p/19q co-deletion status and the tumor grade [2, 3]. Therefore, in 2016 the World Health Organization (WHO) updated its brain tumor classification, categorizing glioma based on these genetic and histological features [4]. In current clinical practice, these features are determined from tumor tissue. While this is not an issue in patients in whom the tumor can be resected, this is problematic when resection can not safely be performed. In these instances, surgical biopsy is performed with the sole purpose of obtaining tissue for diagnosis, which, although relatively safe, is not without risk [5, 6]. Therefore, there has been an increasing interest in complementary non-invasive alternatives that can provide the genetic and histological information used in the WHO 2016 categorization [7, 8].

Magnetic resonance imaging (MRI) has been proposed as a possible candidate because of its non-invasive nature and its current place in routine clinical care [9]. Research has shown that certain MRI features, such as the tumor heterogeneity, correlate with the genetic and histological features of glioma [10, 11]. This notion has popularized, in addition to already popular applications such as tumor segmentation, the use of machine learning methods for the prediction of genetic and histological features, known as radiomics [12, 13, 14]. Although a plethora of such methods now exist, they have found little translation to the clinic [12].

An often discussed challenge for the adoption of machine learning methods in clinical practice is the lack of standardization, resulting in heterogeneity of patient populations, imaging protocols, and scan quality [15, 16]. Since machine learning methods are prone to overfitting, this heterogeneity questions the validity of such methods in a broader patient population [16]. Furthermore, it has

been noted that most current research concerns narrow task-specific methods that lack the context between different related tasks, which might restrict the performance of these methods [17].

An important technical limitation when using deep learning methods is the limited GPU memory, which restricts the size of models that can be trained [18]. This is a problem especially for clinical data, which is often 3D, requiring even more memory than the commonly used 2D networks. This further limits the size of these models resulting in shallower models, and the use of patches of a scan instead of using the full 3D scan as an input, which limits the amount of context these methods can extract from the scans.

Here, we present a new method that addresses the above problems. Our method consists of a single, multi-task convolutional neural network (CNN) that can predict the IDH mutation status, the 1p/19q co-deletion status, and the grade (grade II/III/IV) of a tumor, while also simultaneously segmenting the tumor, see Figure 1. To the best of our knowledge, this is the first method that provides all of this information at the same time, allowing clinical experts to derive the WHO category from the individually predicted genetic and histological features, while also allowing them to consider or disregard specific predictions as they deem fit. Exploiting the capabilities of the latest GPUs, optimizing our implementation to reduce the memory footprint, and using distributed multi-GPU training, we were able to train a model that uses the full 3D scan as an input. We trained our method using the largest, most diverse patient cohort to date, with 1508 patients included from 16 different institutes. To ensure the broad applicability of our method, we used minimal inclusion criteria, only requiring the four most commonly used MRI sequences: pre- and post-contrast T1-weighted (T1w), T2-weighted (T2w), and T2-weighted fluid attenuated inversion recovery (T2w-FLAIR) [19, 20]. No constraints were placed on the patients’ clinical characteristics, such as the tumor grade, or the radiological characteristics of scans, such as the scan quality. In this way, our method could capture the heterogeneity that is naturally present in clinical data. We tested our method on an independent dataset of 240 patients from 13 different institutes, to evaluate the true generalizability of our method. Our results show that we can predict multiple clinical features of glioma from MRI scans in a diverse patient population.

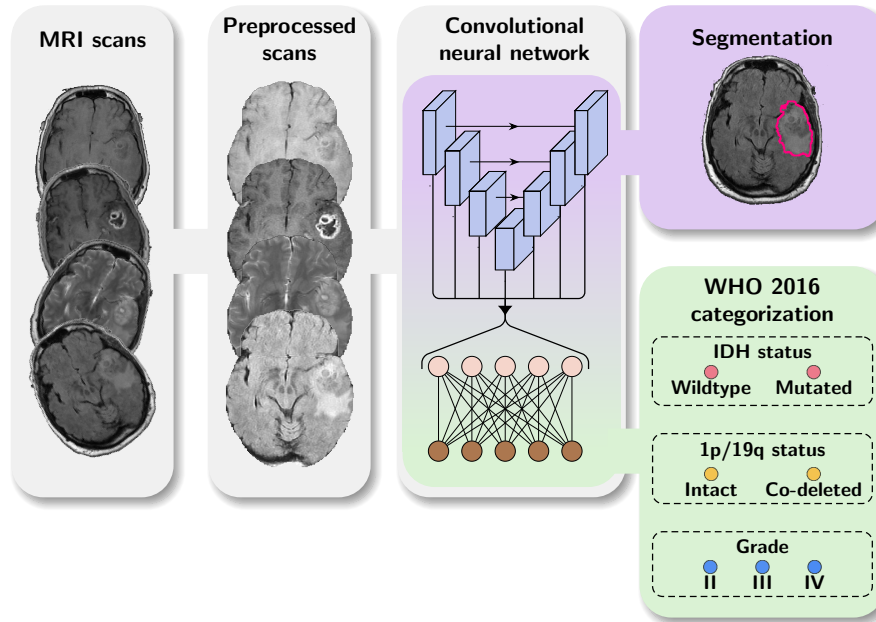


Figure 1: Overview of our method. Pre-, and post-contrast T1w, T2w and T2w-FLAIR scans are used as an input. The scans are registered to an atlas, bias field corrected, skull stripped, and normalized before being passed through our convolutional neural network. One branch of the network segments the tumor, while at the same time the features are combined to predict the IDH status, 1p/19q status, and grade of the tumor.

2 Results

2.1 Patient characteristics

We included a total of 1748 patients in our study, 1508 as a train set and 240 as an independent test set. The patients in the train set originated from nine different data collections and 16 different institutes, and the test set was collected from two different data collections and 13 different institutes. Table 1 provides a full overview of the patient characteristics in the train and test set, and Figure 2 shows the inclusion flowchart and the distribution of the patients over the different data collections in the train set and test set.

Table 1: Patient characteristics for the train set and test set.

	Train set		Test set	
	N	%	N	%
Patients	1508		240	
IDH status				
Mutated	226	15.0	88	36.7
Wildtype	440	29.2	129	53.7
Unknown	842	55.8	23	9.6
1p/19q co-deletion status				
Co-deleted	103	6.8	26	10.8
Intact	337	22.4	207	86.3
Unknown	1068	70.8	7	2.9
Grade				
II	230	15.3	47	19.6
III	114	7.6	59	24.6
IV	830	55.0	132	55.0
Unknown	334	22.1	2	0.8
WHO 2016 categorization				
Oligodendroglioma	96	6.4	26	10.8
Astrocytoma, IDH wildtype	31	2.1	22	9.2
Astrocytoma, IDH mutated	98	6.4	57	23.7
GBM, IDH wildtype	331	21.9	106	44.2
GBM, IDH mutated	16	1.1	5	2.1
Unknown	936	62.1	24	10.0
Segmentation				
Manual	716	47.5	240	100
Automatic	792	52.5	0	0

IDH: isocitrate dehydrogenase, **WHO:** World Health Organization, **GBM:** glioblastoma

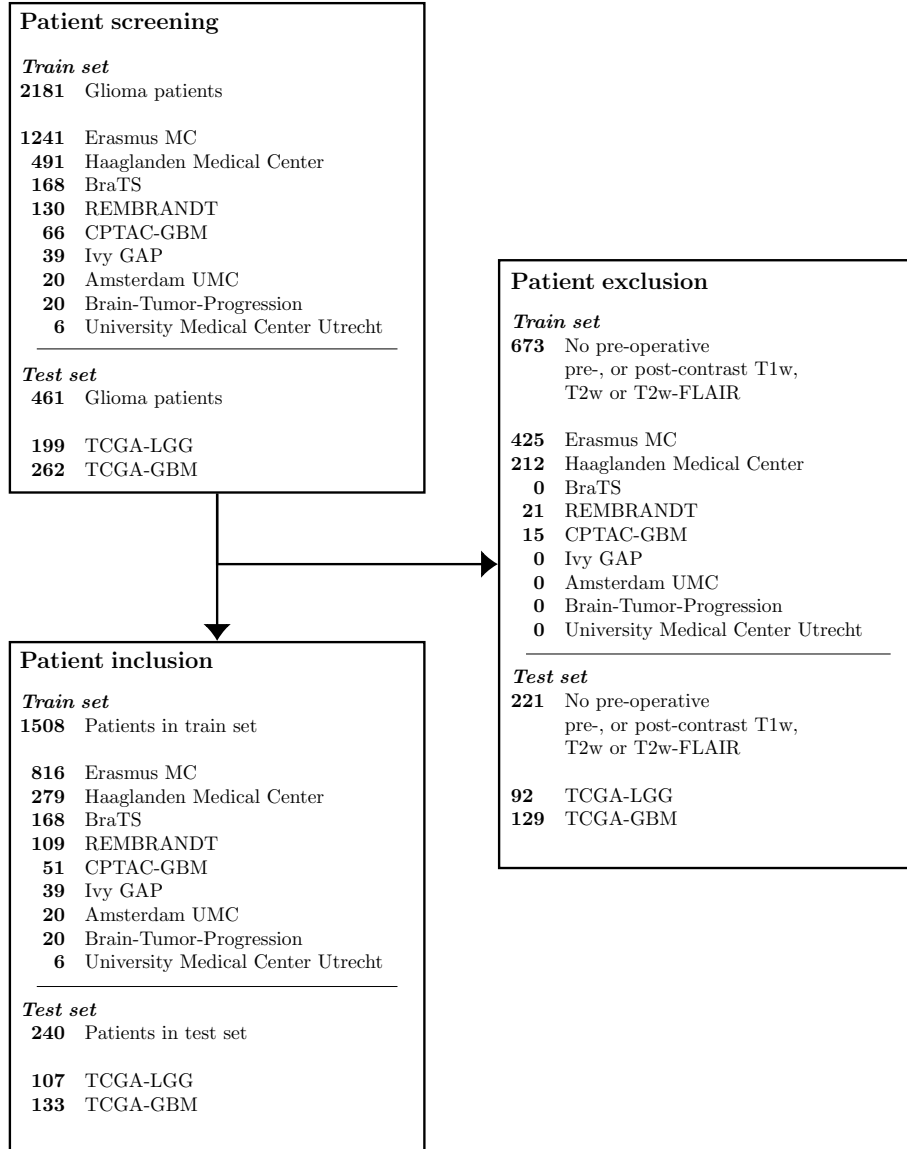


Figure 2: Inclusion flowchart of the train set and test set.

2.2 Algorithm performance

We used 15% of the train set as a validation set and selected the model parameters that achieved the best performance on this validation set, where the model achieved an area under receiver operating characteristic curve (AUC) of 0.88 for the IDH mutation status prediction, an AUC of 0.76 for the 1p/19q co-deletion prediction, an AUC of 0.75 for the grade prediction, and a mean segmentation DICE score of 0.81. The selected model parameters are shown in Appendix F. We then trained a model using these parameters and the full train set, and evaluated it on the independent test set.

For the genetic and histological feature predictions, we achieved an AUC of 0.90 for the IDH mutation status prediction, an AUC of 0.85 for the 1p/19q co-deletion prediction, and an AUC of 0.81 for the grade prediction, in the test set. The full results are shown in Table 2, with the corresponding receiver operating characteristic (ROC)-curves in Figure 3. Table 2 also shows the results in (clinically relevant) subgroups of patients. This shows that we achieved an IDH-AUC of 0.81 in low grade glioma (LGG) (grade II/III), an IDH-AUC of 0.64 in high grade glioma (HGG) (grade IV), and a 1p/19q-AUC of 0.73 in LGG. When only predicting LGG vs. HGG instead of predicting the individual grades, we achieved an AUC of 0.91. In Appendix A we provide confusion matrices for the IDH, 1p/19q, and grade predictions, as well as a confusion matrix for the final WHO 2016 subtype, which shows that only one patient was predicted as a non-existing WHO 2016 subtype. In Appendix C we provide the individual predictions and ground truth labels for all patients in the test set to allow for the calculation of additional metrics.

For the automatic segmentation, we achieved a mean DICE score of 0.84, a mean Hausdorff distance of 18.9 mm, and a mean volumetric similarity coefficient of 0.90. Figure 4 shows boxplots of the DICE scores, Hausdorff distances, and volumetric similarity coefficients for the different patients in the test set. In Appendix B we show five patients that were randomly selected from both the TCGA-LGG and TCGA-GBM data collections, to demonstrate the automatic segmentations made by our method.

2.3 Model interpretability

To provide insight into the behavior of our model we created saliency maps, which show which parts of the scans contributed the most to the prediction. These saliency maps are shown in Figure 5 for two example patients from the test set. It can be seen that for the LGG the network focused on a bright rim in the T2w-FLAIR scan, whereas for the HGG it focused on the enhancement in the post-contrast T1w scan. To aid further interpretation, we provide visualizations of selected filter outputs in the network in Appendix D, which also show that the network focuses on the tumor, and these filters seem to recognize specific imaging features such as the contrast enhancement and T2w-FLAIR brightness.

Table 2: Evaluation results of the final model on the test set.

Patient group	Task	AUC	Accuracy	Sensitivity	Specificity
All	IDH	0.90	0.84	0.72	0.93
	1p/19q	0.85	0.89	0.39	0.95
	Grade (II/III/IV)	0.81	0.71	N/A	N/A
	Grade II	0.91	0.86	0.75	0.89
	Grade III	0.69	0.75	0.17	0.94
	Grade IV	0.91	0.82	0.95	0.66
	LGG vs HGG	0.91	0.84	0.72	0.93
LGG	IDH	0.81	0.74	0.73	0.77
	1p/19q	0.73	0.76	0.39	0.89
HGG	IDH	0.64	0.94	0.40	0.96

Abbreviations: **AUC**: area under receiver operating characteristic curve, **IDH**: isocitrate dehydrogenase, **LGG**: low grade glioma, **HGG**: high grade glioma

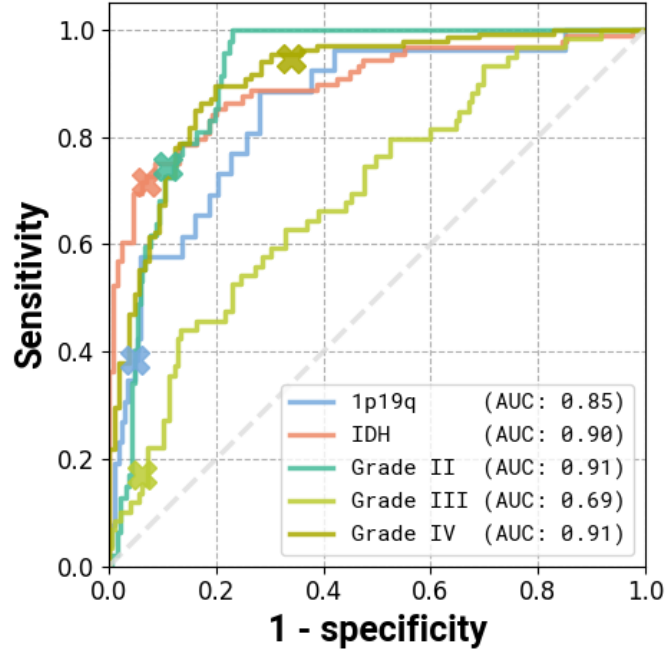


Figure 3: Receiver operating characteristic (ROC)-curves of the genetic and histological features, evaluated on the test set. The crosses indicate the location of the decision threshold for the reported accuracy, sensitivity, and specificity.

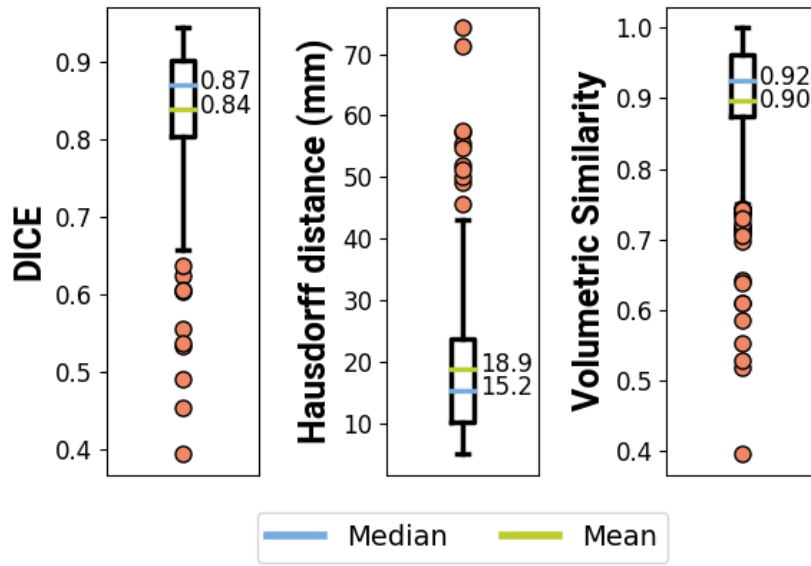
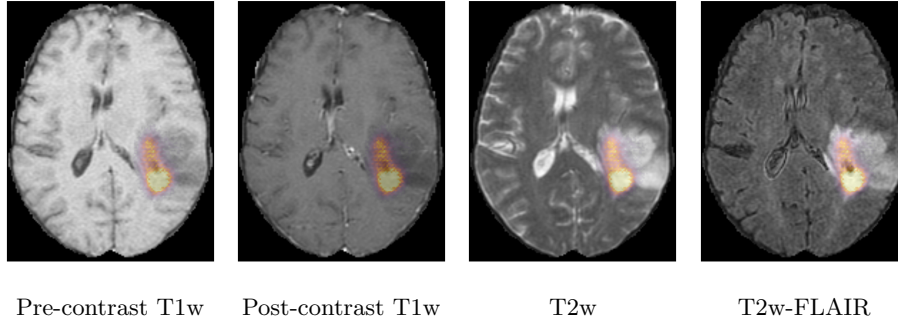
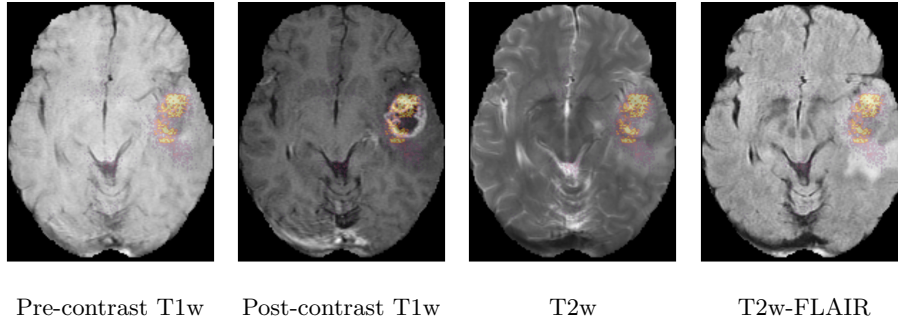


Figure 4: DICE scores, Hausdorff distances, and volumetric similarity coefficients for all patients in the test set. The DICE score is a measure of the overlap between the ground truth and predicted segmentation (where 1 indicates perfect overlap). The Hausdorff distance is a measure of the agreement between the boundaries of the ground truth and predicted segmentation (lower is better). The volumetric similarity coefficient is a measure of the agreement in volume (where 1 indicates perfect agreement).



(a) Saliency maps of a low grade glioma patient (TCGA-DU-6400). This is an IDH mutated, 1p/19q co-deleted, grade II tumor. The network focuses on a rim of brightness in the T2w-FLAIR scan.



(b) Saliency maps of a high grade glioma patient (TCGA-06-0238). This is an IDH wildtype, grade IV tumor. The network focuses on enhancing spots around the necrosis on the post-contrast T1w scan.

Figure 5: Saliency maps of two patients from the test set, showing areas that are relevant for the prediction.

2.4 Model robustness

By not excluding scans from our train set based on radiological characteristics, we were able to make our model robust to low scan quality, as can be seen in an example from the test set in Figure 6. Even though this example scan contained imaging artifacts, our method was able to properly segment the tumor (DICE score of 0.87), and correctly predict the tumor as an IDH wildtype, grade IV tumor.

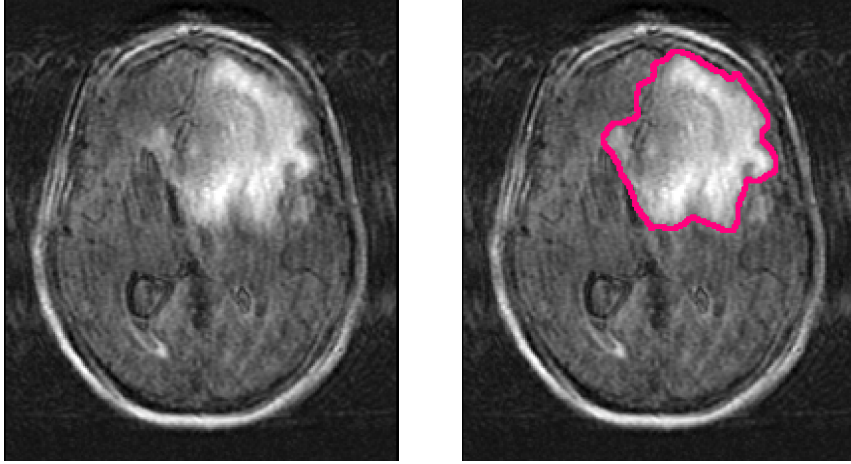
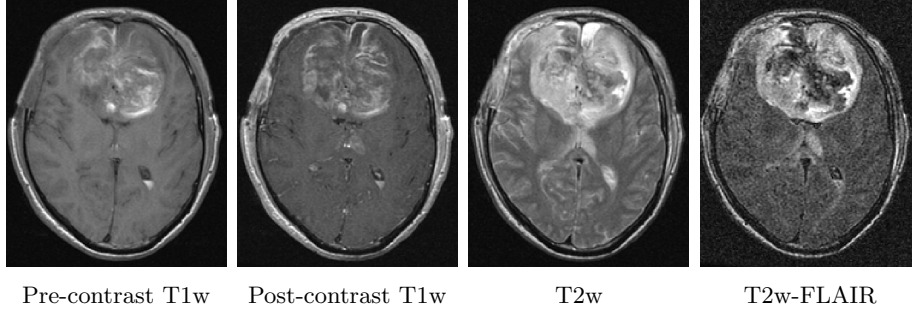
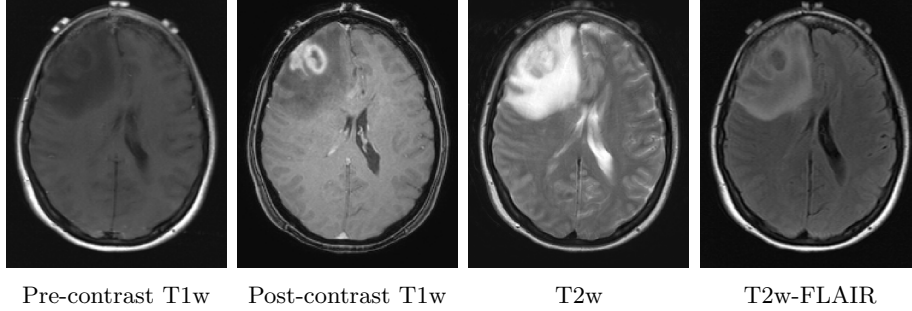


Figure 6: Example of a T2w-FLAIR scan containing imaging artifacts, and the automatic segmentation (red overlay) made by our method. It was correctly predicted as an IDH wildtype, grade IV glioma. This is patient TCGA-06-5408 from the TCGA-GBM collection.

Finally, we considered two examples of scans that were incorrectly predicted by our method, see Figure 7. These two examples were chosen because our network assigned high prediction scores to the wrong classes for these cases. Figure 7a shows an example of a grade II, IDH mutated, 1p/19q co-deleted glioma that was predicted as grade IV, IDH wildtype by our method. Our method’s prediction was most likely caused by the hyperintensities in the post-contrast T1w scan being interpreted as contrast enhancement. Since these hyperintensities are also present in the pre-contrast T1w scan they are most likely calcifications, and the radiological appearance of this tumor is indicative of an oligodendroglioma. Figure 7b shows an example of a grade IV, IDH wildtype glioma that was predicted as a grade III, IDH mutated glioma by our method.



(a) TCGA-DU-6410 from the TCGA-LGG collection. The ground truth histopathological analysis indicated this glioma was grade II, IDH mutated, 1p/19q co-deleted, but our method predicted it as a grade IV, IDH wildtype.



(b) TCGA-76-7664 from the TCGA-HGG collection. Histopathologically this glioma was grade IV, IDH wildtype, but our method predicted it as grade III, IDH mutated.

Figure 7: Examples of scans that were incorrectly predicted by our method.

3 Discussion

We have developed a method that can predict the IDH mutation status, 1p/19q co-deletion status, and grade of glioma, while simultaneously providing the tumor segmentation, based on pre-operative MRI scans. For the genetic and histological feature predictions, we achieved an AUC of 0.90 for the IDH mutation status prediction, an AUC of 0.85 for the 1p/19q co-deletion prediction, and an AUC of 0.81 for the grade prediction, in the test set.

In an independent test set, which contained data from 13 different institutes, we demonstrated that our method predicts these features with good overall performance; we achieved an AUC of 0.90 for the IDH mutation status prediction, an AUC of 0.85 for the 1p/19q co-deletion prediction, and an AUC of 0.81 for the grade prediction, and a mean whole tumor DICE score of 0.84. This performance on unseen data that was only used during the final evaluation of the algorithm, and that was purposefully not used to guide any decisions regarding the method design, shows the true generalizability of our method. Using the latest GPU capabilities we were able to train a large model, which uses the full 3D scan as input. Furthermore, by using the largest, most diverse patient cohort to date we were able to make our method robust to the heterogeneity that is naturally present in clinical imaging data, such that it generalizes for broad application in clinical practice.

By using a multi-task network, our method could learn the context between different features. For example, IDH wildtype and 1p/19q co-deletion are mutually exclusive [21]. If two separate methods had been used, one to predict the IDH status and one to predict the 1p/19q co-deletion status, an IDH wildtype glioma might be predicted to be 1p/19q co-deleted, which does not stroke with the clinical reality. Since our method learns both of these genetic features simultaneously, it correctly learned not to predict 1p/19q co-deletion in tumors that were IDH wildtype; there was only one patient in which our algorithm predicted a tumor to be both IDH wildtype and 1p/19q co-deleted. Furthermore, by predicting the genetic and histological features individually, instead of only predicting the WHO 2016 category, it is possible to adopt updated guidelines such as cIMPACT-NOW, future-proofing our method [22].

Some previous studies also used multi-task networks to predict the genetic and histological features of glioma [23, 24, 25]. Tang et al. [23] used a multi-task network that predicts multiple genetic features, as well as the overall survival of glioblastoma. Since their method only works for glioblastoma patients, the tumor grade must be known in advance, complicating the use of their method in the pre-operative setting when tumor grade is not yet known. Furthermore, their method requires a tumor segmentation prior to application of their method, which is a time-consuming, expert task. In a study by Xue et al. [24], a multi-task network was used, with a structure similar to the one proposed in this paper, to segment the tumor and predict the grade (LGG or HGG) and IDH mutation status. However, they do not predict the 1p/19q co-deletion status needed for the WHO 2016 categorization. Lastly, Decuyper et al. [25] used a multi-task network that predicts the IDH mutation and 1p/19q co-deletion

status, and the tumor grade (LGG or HGG). Their method requires a tumor segmentation as input, which they obtain from a U-Net that is applied earlier in their pipeline; thus, their method requires two networks instead of the single network we use in our method. These differences aside, the most important limitation of each of these studies is the lack of an independent test set for evaluating their results. It is now considered essential that an independent test set is used, to prevent an overly optimistic estimate of a method’s performance [15, 26, 27, 28]. Thus, our study improves on this previous work by providing a single network that combines the different tasks, being trained on a more extensive and diverse dataset, not requiring a tumor segmentation as an input, providing all information needed for the WHO 2016 categorization, and, crucially, by being evaluated in an independent test set.

An important genetic feature that is not predicted by our method is the O⁶-methylguanine-methyltransferase (MGMT) methylation status. Although the MGMT methylation status is not part of the WHO 2016 categorization, it is part of clinical management guidelines and is an important prognostic marker in glioblastoma [4]. In the initial stages of this study, we attempted to predict the MGMT methylation status; however, the performance of this prediction was poor. Furthermore, the methylation cutoff level, which is used to determine whether a tumor is MGMT methylated, shows a wide variety between institutes, leading to inconsistent results [29]. We therefore opted not to include the MGMT prediction at all, rather than to provide a poor prediction of an unsharply defined parameter. Although some methods attempted to predict the MGMT status, with varying degrees of success, there is still an ongoing discussion on the validity of MR imaging features of the MGMT status [23, 30, 31, 32, 33].

Our method shows good overall performance, but there are noticeable performance differences between tumor categories. For example, when our method predicts a tumor as an IDH wildtype glioblastoma, it is correct almost all of the time. On the other hand, it has some difficulty differentiating IDH mutated, 1p/19q co-deleted low-grade glioma from other low-grade glioma. The sensitivity for the prediction of grade III glioma was low, which might be caused by the lack of a central pathology review. Because of this, there were differences in molecular testing and histological analysis, and it is known that distinguishing between grade II and grade III has a poor observer reliability [34]. Although our method can be relevant for certain subgroups, our method’s performance still needs to be improved to ensure relevancy for the full patient population.

In future work, we aim to increase the performance of our method by including perfusion-weighted imaging (PWI) and diffusion-weighted imaging (DWI) since there has been an increasing amount of evidence that these physiological imaging modalities contain additional information that correlates with the tumor’s genetic status and aggressiveness [35, 36]. They were not included in this study since PWI and, to a lesser extent, DWI are not as ingrained in the clinical imaging routine as the structural scans used in this work [19, 20]. Thus, including these modalities would limit our method’s clinical applicability and substantially reduce the number of patients in the train and test set. However,

PWI and DWI are increasingly becoming more commonplace, which will allow including these in future research and which might improve performance.

In conclusion, we have developed a non-invasive method that can predict the IDH mutation status, 1p/19q co-deletion status, and grade of glioma, while at the same time segmenting the tumor, based on pre-operative MRI scans with high overall performance. Although the performance of our method might need to be improved before it will find widespread clinical acceptance, we believe that this research is an important step forward in the field of radiomics. Predicting multiple clinical features simultaneously steps away from the conventional single-task methods and is more in line with the clinical practice where multiple clinical features are considered simultaneously and may even be related. Furthermore, by not limiting the patient population used to develop our method to a selection based on clinical or radiological characteristics, we alleviate the need for a priori (expert) knowledge, which may not always be available. Although steps still have to be taken before radiomics will find its way into the clinic, especially in terms of performance, our work provides a crucial step forward by resolving some of the hurdles of clinical implementation now, and paving the way for a full transition in the future.

4 Methods

4.1 Patient population

The train set was collected from four in-house datasets and five publicly available datasets. In-house datasets were collected from four different institutes: Erasmus MC (EMC), Haaglanden Medical Center (HMC), Amsterdam UMC (AUMC) [37], and University Medical Center Utrecht (UMCU). Four of the five public datasets were collected from The Cancer Imaging Archive (TCIA) [38]: the Repository of Molecular Brain Neoplasia Data (REMBRANDT) collection [39], the Clinical Proteomic Tumor Analysis Consortium Glioblastoma Multiforme (CPTAC-GBM) collection [40], the Ivy Glioblastoma Atlas Project (Ivy GAP) collection [41, 42], and the Brain-Tumor-Progression collection [43]. The fifth dataset was the 2019 Brain Tumor Segmentation challenge (BraTS) challenge dataset [44, 45, 46], from which we excluded the patients that were also available in the TCGA-LGG and TCGA-GBM collections [47, 48].

For the internal datasets from the EMC and the HMC, manual segmentations were available, which were made by four different clinical experts. For patients where segmentations from more than one observer were available, we randomly picked one of the segmentations to use in the train set. The segmentations from the AUMC data were made by a single observer of the study by Visser et al. [37]. From the public datasets, only the BraTS dataset and the Brain-Tumor-Progression dataset provided manual segmentations. Segmentations of the BraTS dataset, as provided in the 2019 training and validation set were used. For the Brain-Tumor-Progression dataset, the segmentations as provided in the TCIA data collection were used.

Patients were included if pre-operative pre- and post-contrast T1w, T2w, and T2w-FLAIR scans were available; no further inclusion criteria were set. For example, patients were not excluded based on the radiological characteristics of the scan, such as low imaging quality or imaging artifacts, or the glioma’s clinical characteristics such as the grade. If multiple scans of the same contrast type were available in a single scan session (e.g., multiple T2w scans), the scan upon which the segmentation was made was selected. If no segmentation was available, or the segmentation was not made based on that scan contrast, the scan with the highest axial resolution was used, where a 3D acquisition was preferred over a 2D acquisition.

For the in-house data, genetic and histological data were available for the EMC, HMC, and UMCU dataset, which were obtained from analysis of tumor tissue after biopsy or resection. Genetic and histological data of the public datasets were also available for the REMBRANDT, CPTAC-GBM, and Ivy GAP collections. Data for the REMBRANDT and CPTAC-GBM collections was collected from the clinical data available at the TCIA [40, 39]. For the Ivy GAP collection, the genetic and histological data were obtained from the Swedish Institute at <https://ivygap.swedish.org/home>.

As a test set we used the TCGA-LGG and TCGA-GBM collections from the TCIA [47, 48]. Genetic and histological labels were obtained from the clinical data available at the TCIA. Segmentations were used as available from the TCIA, based on the 2018 BraTS challenge [45, 49, 50]. The inclusion criteria for the patients included in the BraTS challenge were the same as our inclusion criteria: the presence of a pre-operative pre- and post-contrast T1w, T2w, and T2w-FLAIR scan. Thus, patients from the TCGA-LGG and TCGA-GBM were included if a segmentation from the BraTS challenge was available. However, for three patients, we found that although they did have manual segmentations, they did not meet our inclusion requirements: TCGA-08-0509 and TCGA-08-0510 from TCGA-GBM because they did not have a pre-contrast T1w scan and TCGA-FG-7634 from TCGA-LGG because there was no post-contrast T1w scan.

4.2 Automatic segmentation in the train set

To present our method with a large diversity in scans, we wanted to include as many patients in the train set as possible from the different datasets. Therefore, we performed automatic segmentation in patients that did not have manual segmentations. To this end, we used an initial version of our network (presented in Section 4.4), without the additional layers that were needed for the prediction of the genetic and histological features. This network was initially trained using all patients in the train set for whom a manual segmentation was available, and this trained network was then applied to all patients for which a manual segmentation was not available. The resulting automatic segmentations were inspected, and if their quality was acceptable, they were added to the train set. The network was then trained again, using this increased dataset, and was applied to scans that did not yet have a segmentation of acceptable quality.

This process was repeated until an acceptable segmentation was available for all patients, which constituted our final, complete train set.

4.3 Pre-processing

For all datasets, except for the BraTS dataset for which the scans were already provided in NIfTI format, the scans were converted from DICOM format to NIfTI format using dcm2niix version v1.0.20190410 [51]. We then registered all scans to the MNI152 T1w and T2w atlases, version ICBM 2009a, which had a resolution of $1 \times 1 \times 1 \text{ mm}^3$ and a size of $197 \times 233 \times 189$ voxels [52, 53]. The scans were affinely registered using Elastix 5.0 [54, 55]. The pre- and post-contrast T1w scans were registered to the T1w atlas; the T2w and T2w-FLAIR scans were registered to the T2w atlas. When a manual segmentation was available for patients from the in-house datasets, the registration parameters that resulted from registering the scan used during the segmentation were used to transform the segmentation to the atlas. In the case of the public datasets, we used the registration parameters of the T2w-FLAIR scans to transform the segmentations.

After the registration, all scans were N4 bias field corrected using SimpleITK version 1.2.4 [56]. A brain mask was made for the atlas using HD-BET, both for the T1w atlas and the T2w atlas [57]. This brain mask was used to skull strip all registered scans and crop them to a bounding box around the brain mask, reducing the amount of background present in the scans, resulting in a scan size of $152 \times 182 \times 145$ voxels. Subsequently, the scans were normalized such that for each scan, the average image intensity was 0, and the standard deviation of the image intensity was 1 within the brain mask. Finally, the background outside the brain mask was set to the minimum intensity value within the brain mask.

Since the segmentation could sometimes be rugged at the edges after registration, especially when the segmentations were initially made on low-resolution scans, we smoothed the segmentation using a $3 \times 3 \times 3$ median filter (this was only done in the train set). For segmentations that contained more than one label, e.g., when the tumor necrosis and enhancement were separately segmented, all labels were collapsed into a single label to obtain a single segmentation of the whole tumor. The genetic and histological labels and the segmentations of each patient were one-hot encoded. The four scans, ground truth labels, and segmentation of each patient were then used as the input to the network.

4.4 Model

We based the architecture of our model on the U-Net architecture, with some adaptations made to allow for a full 3D input and the auxiliary tasks [58]. Our network architecture, which we have named PrognosAIs Structure-Net, or PS-Net for short, can be seen in Figure 8.

To use the full 3D scan as an input to the network, we replaced the first pooling layer that is usually present in the U-Net with a strided convolution, with a kernel size of $9 \times 9 \times 9$ and a stride of $3 \times 3 \times 3$. In the upsampling branch of

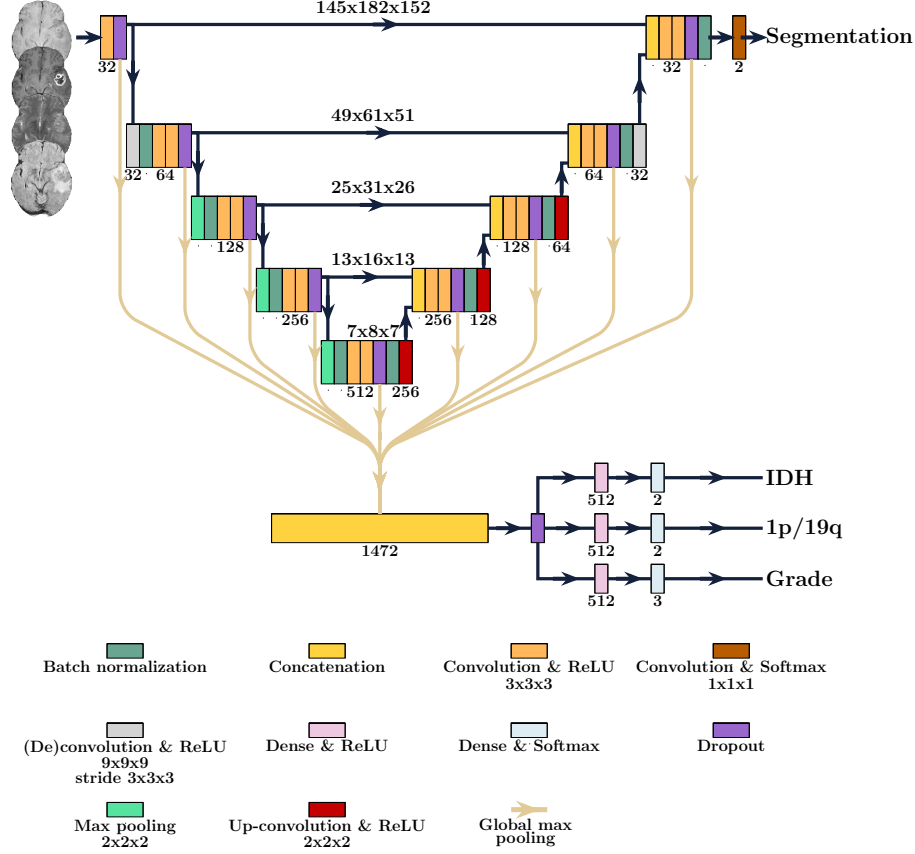


Figure 8: Overview of the PrognosAIs Structure-Net (PS-Net) architecture used for our model. The numbers below the different layers indicate the number of filters, dense units or features at that layer. We have also indicated the feature map size at the different depths of the network.

the network, the last up-convolution is replaced by a deconvolution, with the same kernel size and stride.

At each depth of the network, we have added global max-pooling layers directly after the dropout layer, to obtain imaging features that can be used to predict the genetic and histological features. We chose global pooling layers as they do not introduce any additional parameters that need to be trained, thus keeping the memory required by our model manageable. The features from the different depths of the network were concatenated and fed into three different dense layers, one for each of the genetic and histological outputs.

l_2 kernel regularization was used in all convolutional layers, except for the last convolutional layer used for the output of the segmentation. In total this model contained 27,042,473 trainable and 2,944 non-trainable parameters.

4.5 Model training

Training of the model was done on eight NVidia RTX2080Ti’s with 11GB of memory, using TensorFlow 2.2.0 [59]. To be able to use the full 3D scan as input to the network, without running into memory issues, we had to optimize the memory efficiency of the model training. Most importantly, we used mixed-precision training, which means that most of the variables of the model (such as the weights) were stored in float16, which requires half the memory of float32, which is typically used to store these variables [60]. Only the last softmax activation layers of each output were stored as float32. We also stored our pre-processed scans as float16 to further reduce memory usage.

However, even with these settings, we could not use a batch size larger than 1. It is known that a larger batch size is preferable, as it increases the stability of the gradient updates and allows for a better estimation of the normalization parameters in batch normalization layers [61]. Therefore, we distributed the training over the eight GPUs, using the NCCL AllReduce algorithm, which combines the gradients calculated on each GPU before calculating the update to the model parameters [62]. We also used synchronized batch normalization layers, which synchronize the updates of their parameters over the distributed models. In this way, our model had a virtual batch size of eight for the gradient updates and the batch normalization layers parameters.

To provide more samples to the algorithm and prevent potential overtraining, we applied four types of data augmentation during training: cropping, rotation, brightness shifts, and contrast shifts. Each augmentation was applied with a certain augmentation probability, which determined the probability of that augmentation type being applied to a specific sample. When an image was cropped, a random number of voxels between 0 and 20 was cropped from each dimension, and filled with zeros. For the random rotation, an angle between -30° and 30° degrees was selected from a uniform distribution for each dimension. The brightness shift was applied with a delta uniformly drawn between 0 and 0.2, and the contrast shift factor was randomly drawn between 0.85 and 1.15. We also introduced an augmentation factor, which determines how often each sample was parsed as an input sample during a single epoch, where each time it could be augmented differently.

For the IDH, 1p/19q, and grade output, we used a masked categorical cross-entropy loss, and for the segmentation we used a DICE loss, see Appendix E for details. We used AdamW as an optimizer, which has shown improved generalization performance over Adam by introducing the weight decay parameter as a separate parameter from the learning rate [63]. The learning rate was automatically reduced by a factor of 0.25 if the loss did not improve during the last five epochs, with a minimum learning rate of $1 \cdot 10^{-11}$. The model could train for a maximum of 150 epochs, and training was stopped early if the average loss over the last five epochs did not improve. Once the model was finished training, the weights from the epoch with the lowest loss were restored.

4.6 Hyperparameter tuning

Hyperparameters involved in the training of the model needed to be tuned to achieve the best performance. We tuned a total of six hyper parameters: the l_2 -norm, the dropout rate, the augmentation factor, the augmentation probability, the optimizer’s initial learning rate and the optimizer’s weight decay. A full overview of the trained parameters and the values tested for the different settings is presented in Appendix F.

To tune these hyperparameters, we split the train set into a hyperparameter training set (85%/1282 patients of the full train data) and a hyperparameter validation set (15%/226 patients of the full train data). Models were trained for different hyperparameter settings via an exhaustive search using the hyperparameter train set, and then evaluated on the hyperparameter validation set. No data augmentation was applied to the hyperparameter validation to ensure that results between trained models were comparable. The hyperparameters that led to the lowest overall loss in the hyperparameter validation set were chosen as the optimal hyperparameters. We trained the final model using these optimal hyperparameters and the full train set.

4.7 Post-processing

The predictions of the network were post-processed to obtain the final predicted labels and segmentations for the samples. Since softmax activations were used for the genetic and histological outputs, a prediction between 0 and 1 was outputted for each class, where the individual predictions summed to 1. The final predicted label was then considered as the class with the highest prediction score. For the prediction of LGG (grade II/III) vs. HGG (grade IV), the prediction scores of grade II and grade III were combined to obtain the prediction score for LGG, the prediction score of grade IV was used as the prediction score for HGG. If a segmentation contained multiple unconnected components, we only retained the largest component to obtain a single whole tumor segmentation.

4.8 Model evaluation

The performance of the final trained model was evaluated on the independent test set, comparing the predicted labels with the ground truth labels. For the genetic and histological features, we evaluated the AUC, the accuracy, the sensitivity, and the specificity using scikit-learn version 0.23.1, for details see Appendix G [64]. We evaluated these metrics on the full test set and in subcategories relevant to the WHO 2016 guidelines. We evaluated the IDH performance separately in the LGG (grade II/III) and HGG (grade IV) subgroups, the 1p/19q performance in LGG, and we also evaluated the performance of distinguishing between LGG and HGG instead of predicting the individual grades.

To evaluate the performance of the segmentation, we calculated the DICE scores, Hausdorff distances, and volumetric similarity coefficient comparing the automatic segmentation of our method and the manual ground truth segmen-

tations for all patients in the test set. These metrics were calculated using the EvaluateSegmentation toolbox, version 2017.04.25 [65], for details see Appendix G.

To prevent an overly optimistic estimation of our model’s predictive value, we only evaluated our model on the test set once all hyperparameters were chosen, and the final model was trained. In this way, the performance in the test set did not influence decisions made during the development of the model, preventing possible overfitting by fine-tuning to the test set.

To gain insight into the model, we made saliency maps that show which parts of the scan contribute the most to the prediction of the CNN [66]. Saliency maps were made using tf-keras-vis 0.5.2, changing the activation function of all output layers from softmax to linear activations, using SmoothGrad to reduce the noisiness of the saliency maps [66].

Another way to gain insight into the network’s behavior is to visualize the filter outputs of the convolutional layers, as they can give some idea as to what operations the network applies to the scans. We visualized the filter outputs of the last convolutional layers in the downsample and upsample path at the first depth (at an image size of 49x61x51) of our network. These filter outputs were visualized by passing a sample through the network and showing the convolutional layers’ outputs, replacing the ReLU activation with linear activations.

4.9 Data availability

An overview of the patients included from the public datasets used in the training and testing of the algorithm, and their ground truth label is available in Appendix H. The data from the public datasets are available in TCIA under DOIs: 10.7937/K9/TCIA.2015.588OZUZB, 10.7937/k9/tcia.2018.3rje41q1, 10.7937/K9/TCIA.2016.XLwaN6nL, and 10.7937/K9/TCIA.2018.15quzvnb. Data from the BraTS are available at <http://braintumorsegmentation.org/>. Data from the in-house datasets are not publicly available due to participant privacy and consent.

4.10 Code availability

The code used in this paper is available on GitHub under an Apache 2 license at https://github.com/Svdvoort/PrognosAIs_glioma. This code includes the full pipeline from registration of the patients to the final post-processing of the predictions. The trained model is also available on GitHub, along with code to apply it to new patients.

Appendices

A Confusion matrices

Tables 3, 4 and 5 show the confusion matrices for the IDH, 1p/19q, and grade predictions, and Table 6 shows the confusion matrix for the WHO 2016 subtypes.

Table 4 shows that the algorithm mainly has difficulty recognizing 1p/19q co-deleted tumors, which are mostly predicted as 1p/19q intact. Table 5 shows that most of the incorrectly predicted grade III tumors are predicted as grade IV tumors.

Table 6 shows that our algorithm often incorrectly predicts IDH-wildtype astrocytoma as IDH-wildtype glioblastoma. The latest cIMPACT-NOW guidelines propose a new categorization, in which IDH-wildtype astrocytoma that show either TERT promoter methylation, or EGFR gene amplification, or chromosome 7 gain/chromosome 10 loss are classified as IDH-wildtype glioblastoma [22]. This new categorization is proposed since the survival of patients with those IDH-wildtype astrocytoma is similar to the survival of patients with IDH-wildtype glioblastoma [22]. From the 13 IDH-wildtype astrocytoma that were wrongly predicted as IDH-wildtype glioblastoma, 12 would actually be categorized as IDH-wildtype glioblastoma under this new categorization. Thus, although our method wrongly predicted the WHO 2016 subtype, it might actually have picked up on imaging features related to the aggressiveness of the tumor, which might lead to a better categorization.

Table 3: Confusion matrix of the IDH predictions.

		Predicted	
		Wildtype	Mutated
Actual	Wildtype	120	9
	Mutated	25	63

Table 4: Confusion matrix of the 1p/19q predictions.

		Predicted	
		Intact	Co-deleted
Actual	Intact	197	10
	Co-deleted	16	10

Table 5: Confusion matrix of the grade predictions.

		Predicted		
		Grade II	Grade III	Grade IV
Actual	Grade II	35	6	6
	Grade III	19	10	30
	Grade IV	2	5	125

Table 6: Confusion matrix of the WHO 2016 predictions. The 'other' category indicates patients that were predicted as a non-existing WHO 2016 subtype, for example IDH wildtype, 1p/19q co-deleted tumors. Only one patient (TCGA-HT-A5RC) was predicted as a non-existing category. It was predicted as an IDH wildtype, 1p/19q co-deleted, grade IV tumor.

		Predicted					
		Oligodendroglioma	IDH-mutated astrocytoma	IDH-wildtype astrocytoma	IDH-mutated glioblastoma	IDH-wildtype glioblastoma	Other
Actual	Oligodendroglioma	10	8	1	0	7	0
	IDH-mutated astrocytoma	6	34	4	3	10	0
	IDH-wildtype astrocytoma	1	2	3	2	13	1
	IDH-mutated glioblastoma	0	1	0	0	3	0
	IDH-wildtype glioblastoma	0	3	3	1	96	0

Oligodendroglioma are IDH-mutated, 1p/19q co-deleted, grade II/III glioma.

IDH-mutated astrocytoma are IDH-mutated, 1p/19q intact, grade II/III glioma.

IDH-wildtype astrocytoma are IDH-wildtype, 1p/19q intact, grade II/III glioma.

IDH-mutated glioblastoma are IDH-mutated, grade IV glioma.

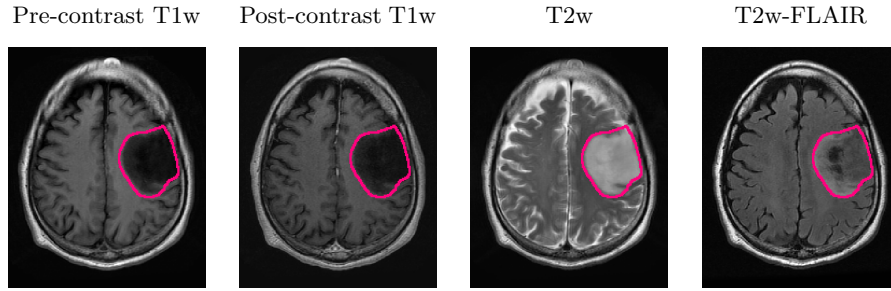
IDH-wildtype glioblastoma are IDH-wildtype, grade IV glioma.

B Segmentation examples

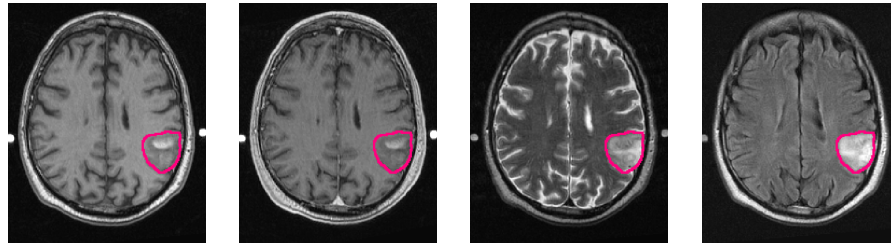
To demonstrate the automatic segmentations made by our method, we randomly selected five patients from both the TCGA-LGG and the TCGA-GBM dataset. The scans and segmentations of the five patients from the TCGA-LGG dataset and the TCGA-GBM dataset are shown in Figures 9 and 10, respectively. The DICE score, Hausdorff distance, and volumetric similarity coefficient for these patients are given in Table 7. The method seems to mostly focus on the hyperintensities of the T2w-FLAIR scan. Despite the registrations issues that can be seen for the T2w scan in Figure 10d the tumor was still properly segmented, demonstrating the robustness of our method.

Patient	DICE	HD (mm)	VSC
TCGA-LGG			
TCGA-DU-7301	0.89	10.3	0.95
TCGA-FG-5964	0.80	5.8	0.82
TCGA-FG-A713	0.73	7.8	0.88
TCGA-HT-7475	0.87	14.9	0.90
TCGA-HT-8106	0.88	11.2	0.99
TCGA-GBM			
TCGA-02-0037	0.82	22.6	0.99
TCGA-08-0353	0.91	13.0	0.98
TCGA-12-1094	0.90	7.3	0.93
TCGA-14-3477	0.90	16.5	0.99
TCGA-19-5951	0.73	19.7	0.73

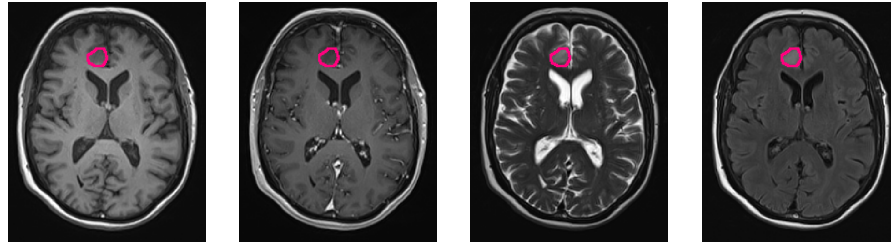
Table 7: The DICE score, Hausdorff distance (HD), and volumetric similarity coefficient (VSC) for the randomly selected patients from the TCGA-LGG and TCGA-GBM data collections.



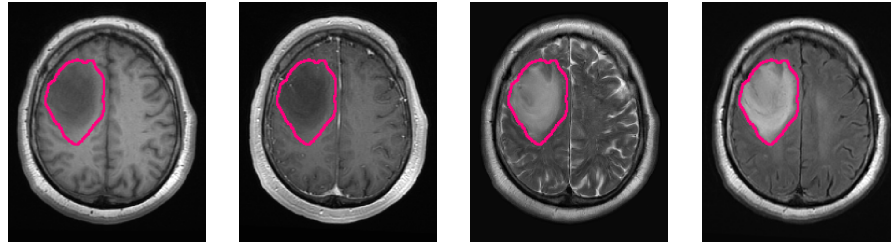
(a) Patient TCGA-DU-7301 from the TCGA-LGG data collection.



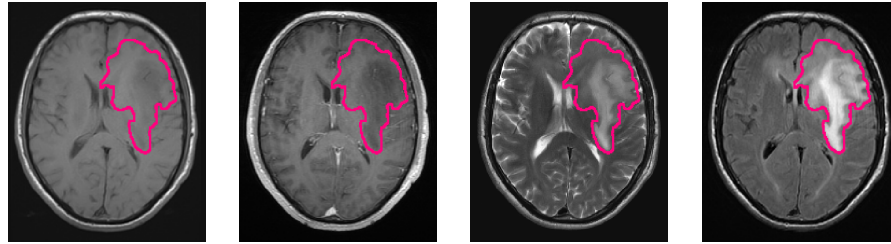
(b) Patient TCGA-FG-5964 from the TCGA-LGG data collection.



(c) Patient TCGA-FG-A713 from the TCGA-LGG data collection.

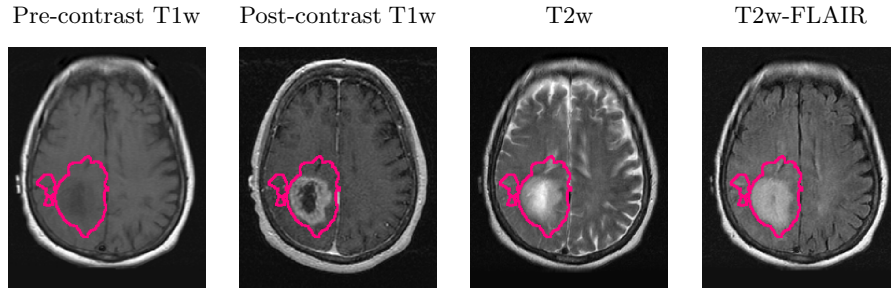


(d) Patient TCGA-HT-7475 from the TCGA-LGG data collection.

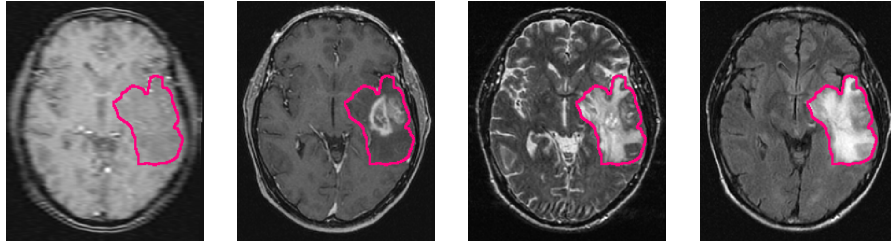


(e) Patient TCGA-HT-8106 from the TCGA-LGG data collection.

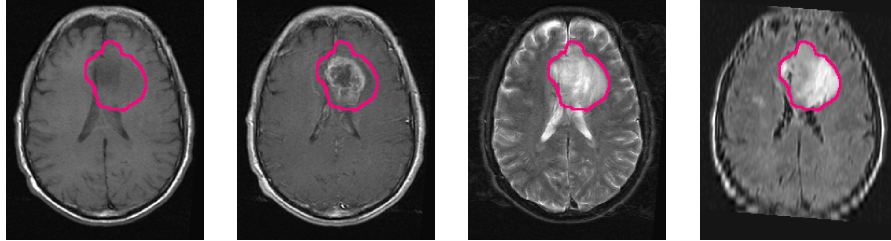
Figure 9: Examples of scans and automatic segmentations of five patients that were randomly selected from the TCGA-LGG data collection.



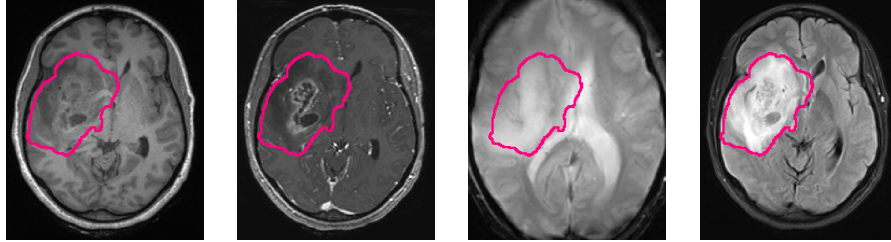
(a) Patient TCGA-02-0037 from the TCGA-GBM data collection.



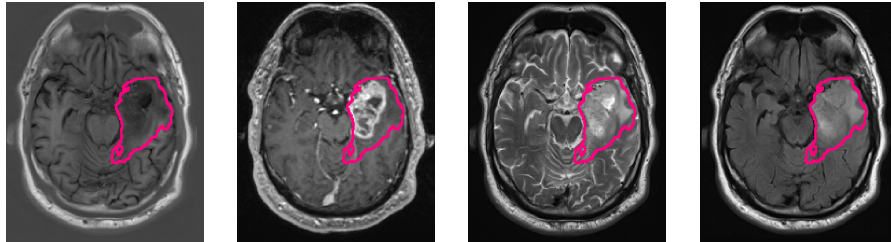
(b) Patient TCGA-08-0353 from the TCGA-GBM data collection.



(c) Patient TCGA-12-1094 from the TCGA-GBM data collection.



(d) Patient TCGA-14-3477 from the TCGA-GBM data collection.



(e) Patient TCGA-19-5951 from the TCGA-GBM data collection.

Figure 10: Examples of scans and automatic segmentations of five patients that were randomly selected from the TCGA-GBM data collection.

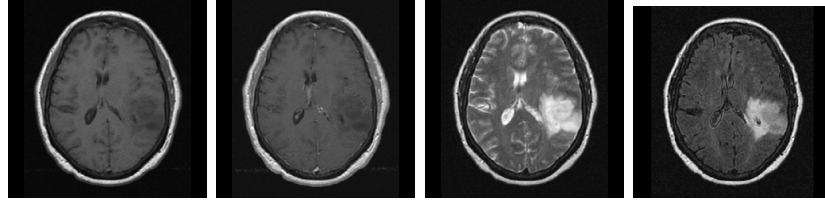
C Prediction results in the test set

[Supplementary file](#)

D Filter output visualizations

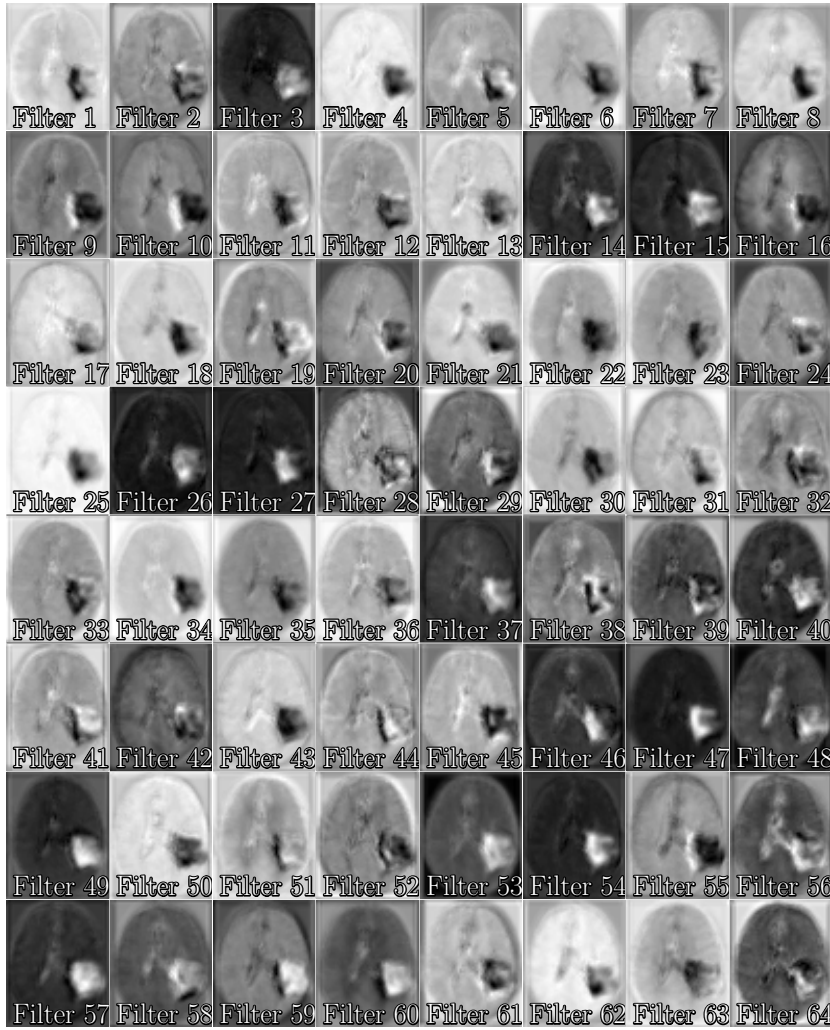
Figures 11 and 12 show the output of the convolution filters for the same LGG patient as shown in Figure 5a, and Figures 13 and 14 show the output of the convolution filters for the same HGG patient as shown in Figure 5b. Figures 11 and 13 show the outputs of the last convolution layer in the downsample path at the feature size of $49 \times 61 \times 51$ (the fourth convolutional layer in the network). Figures 12 and 14 show the outputs of the last convolution layer in the upsample path at the feature size of $49 \times 61 \times 51$ (the nineteenth convolutional layer in the network).

Comparing Figure 11 to Figure 12 and Figure 13 to Figure 14 we can see that the convolutional layers in the upsample path do not keep a lot of detail for the healthy part of the brain, as this region seems blurred. However, within the tumor different regions can still be distinguished. The different parts of the tumor from the scans can also be seen, such as the contrast-enhancing part and the high signal intensity on the T2w-FLAIR. For the grade IV glioma in Figure 14, some filters, such as filter 26, also seem to focus on the necrotic part of the tumor.



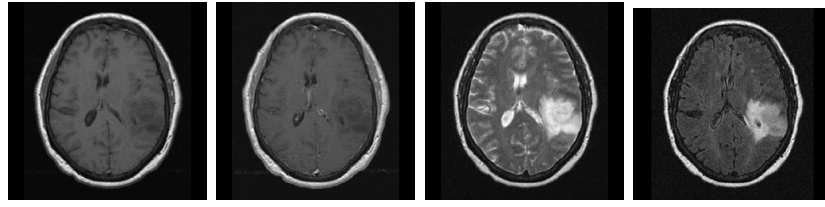
Pre-contrast T1w Post-contrast T1w T2w T2w-FLAIR

(a) Scans used to derive the convolutional layer filter output visualizations.



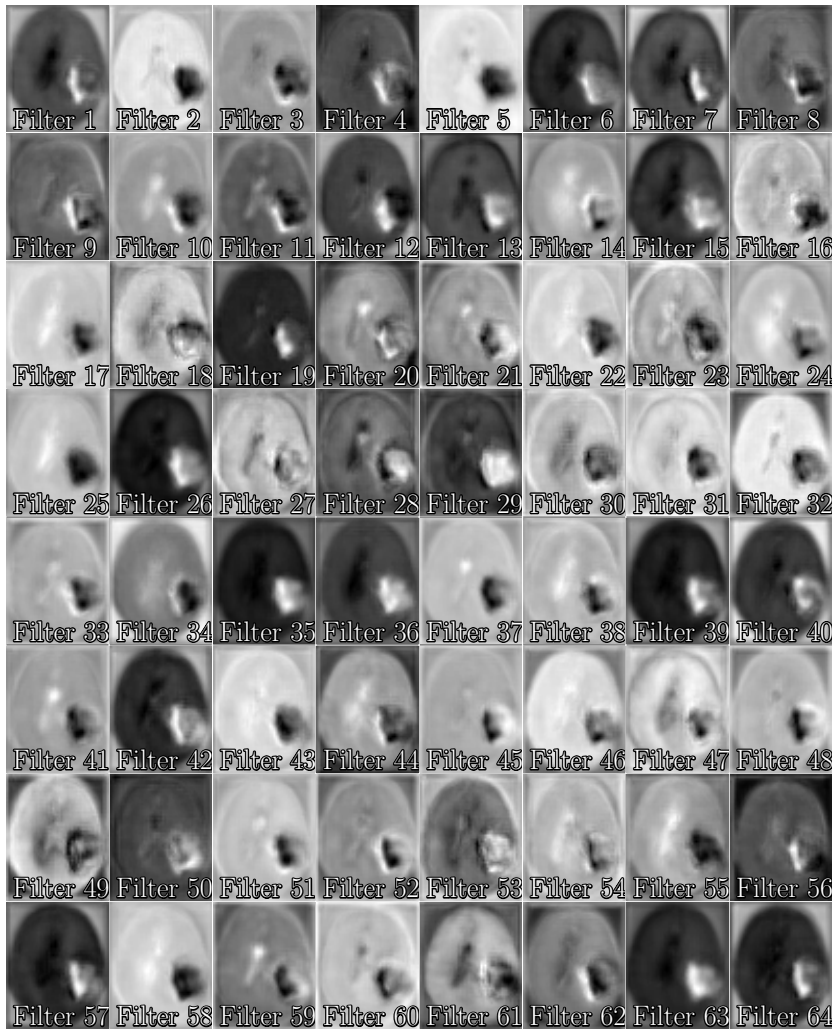
(b) Filter output visualizations.

Figure 11: Filter output visualizations of the last convolutional layer in the downsample path of the network at feature map size 49x61x51 for patient TCGA-DU-6400. This is an IDH mutated, 1p/19q co-deleted, grade II glioma.



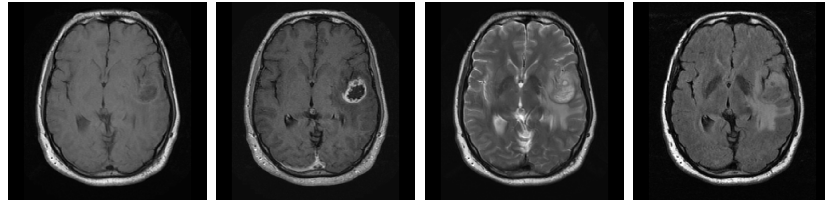
Pre-contrast T1w Post-contrast T1w T2w T2w-FLAIR

(a) Scans used to derive the convolutional layer filter output visualizations.



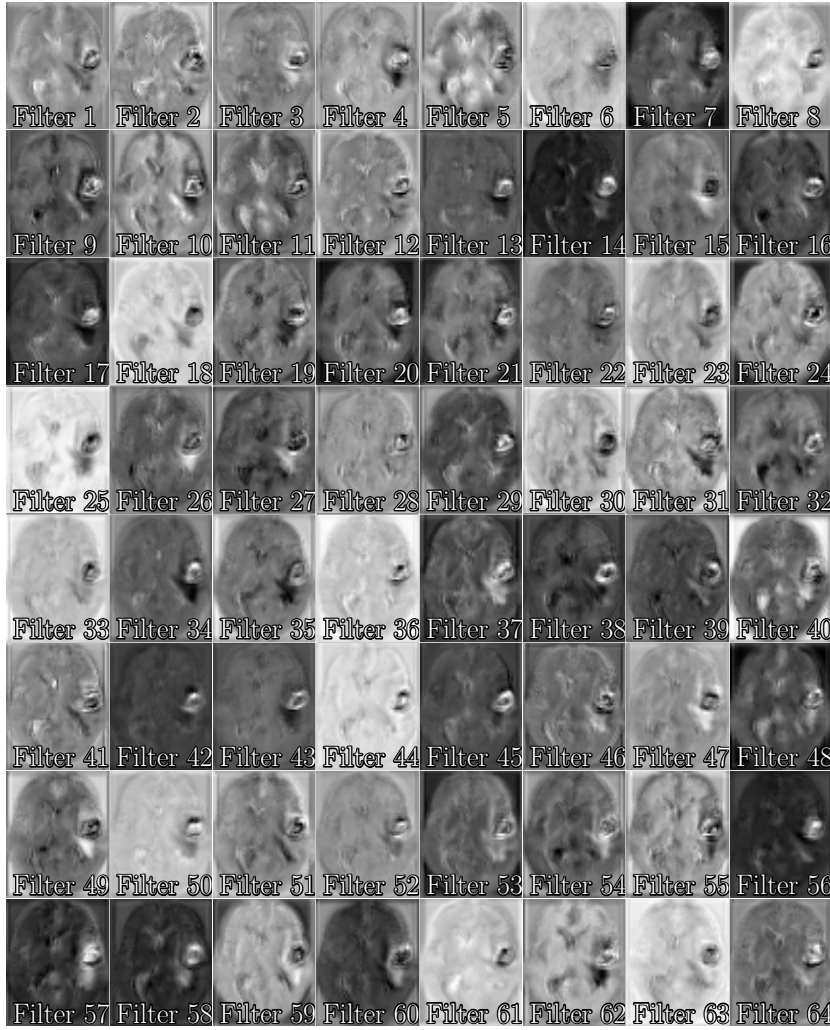
(b) Filter output visualizations.

Figure 12: Filter output visualizations of the last convolutional layer in the upsample path of the network at feature map size 49x61x51 for patient TCGA-DU-6400. This is an IDH mutated, 1p/19q co-deleted, grade II glioma.



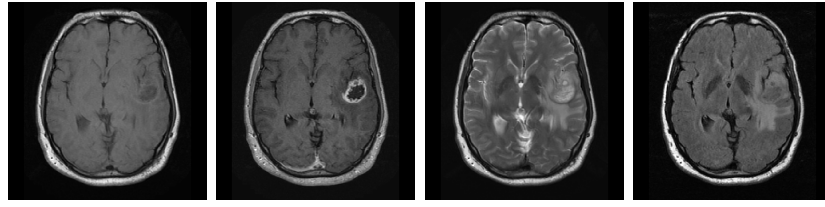
Pre-contrast T1w Post-contrast T1w T2w T2w-FLAIR

(a) Scans used to derive the convolutional layer filter output visualizations.



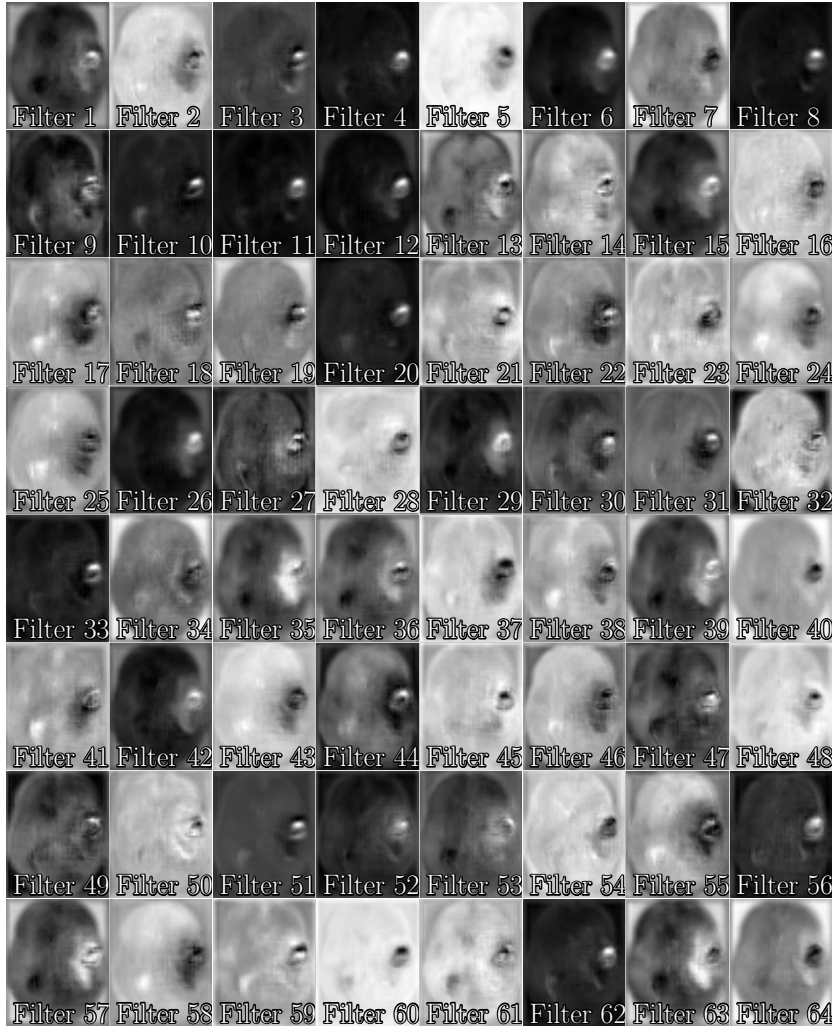
(b) Filter output visualizations.

Figure 13: Filter output visualizations of the last convolutional layer in the downsample path of the network at feature map size $49 \times 61 \times 51$ for patient TCGA-06-0238. This is an IDH wildtype, grade IV glioma.



Pre-contrast T1w Post-contrast T1w T2w T2w-FLAIR

(a) Scans used to derive the convolutional layer filter output visualizations.



(b) Filter output visualizations.

Figure 14: Filter output visualizations of the last convolutional layer in the upsample path of the network at feature map size $49 \times 61 \times 51$ for patient TCGA-06-0238. This is an IDH wildtype, grade IV glioma.

E Training losses

During the training of the network we used masked categorical cross-entropy loss for the IDH, 1p/19q, and grade outputs. The normal categorical cross-entropy loss is defined as:

$$\mathcal{L}_{batch}^{CE} = -\frac{1}{N_{batch}} \sum_j \sum_{i \in C} y_{i,j} \log(\hat{y}_{i,j}), \quad (1)$$

where \mathcal{L}_{batch}^{CE} is the total cross-entropy loss over a batch, $y_{i,j}$ is the ground truth label of sample j for class i , $\hat{y}_{i,j}$ is the prediction score for sample j for class i , C is the set of classes, and N_{batch} is the number of samples in the batch. Here it is assumed that the ground truth labels are one-hot-encoded, thus $y_{i,j}$ is either 0 or 1 for each class. In our case, the ground truth is not known for all samples, which can be incorporated in Equation (1) by setting $y_{i,j}$ to 0 for all classes for a sample for which the ground truth is not known. That sample would then not contribute to the overall loss, and would not contribute to the gradient update. However, this can skew the total loss over a batch, since the loss is still averaged over the total number of samples in a batch, regardless of whether the ground truth is known, resulting in a lower loss for batches that contained more samples with unknown ground truth. Therefore, we used a masked categorical cross-entropy loss:

$$\mathcal{L}_{batch}^{CE} = -\frac{1}{N_{batch}} \sum_j \mu_j^{batch} \sum_{i \in C} y_{i,j} \log(\hat{y}_{i,j}), \quad (2)$$

where

$$\mu_j^{batch} = \frac{N_{batch}}{\sum_{i,j} y_{i,j}} \sum_i y_{i,j} \quad (3)$$

is the batch weight for sample j . In this way, the total batch loss is only averaged over the samples that actually have a ground truth.

Since there was an imbalance between the number of ground truth samples for each class, we used class weights to compensate for this imbalance. Thus, the loss becomes:

$$\mathcal{L}_{batch}^{CE} = -\frac{1}{N_{batch}} \sum_j \mu_j^{batch} \sum_{i \in C} \mu_i^{class} y_{i,j} \log(\hat{y}_{i,j}), \quad (4)$$

where

$$\mu_i^{class} = \frac{N}{N_i |C|} \quad (5)$$

is the class weight for class i , N is the total number of samples with known ground truth, N_i is the number of samples of class i , and $|C|$ is the number of classes. By determining the class weight in this way, we ensured that:

$$\mu_i^{class} N_i = \frac{N}{|C|} = \text{constant}. \quad (6)$$

Thus, each class would have the same contribution to the overall loss. These class weights were (individually) determined for the IDH output, the 1p/19q output, and the grade output.

For the segmentation output we used the DICE loss:

$$\mathcal{L}_{batch}^{DICE} = \sum_j 1 - 2 \cdot \frac{\sum_k^{voxels} y_{j,k} \cdot \hat{y}_{j,k}}{\sum_k^{voxels} y_{j,k} + \hat{y}_{j,k}}, \quad (7)$$

where $y_{j,k}$ is the ground truth label in voxel k of sample j , and $\hat{y}_{j,k}$ is the prediction score outputted for voxel k of sample j .

The total loss that was optimized for the model was a weighted sum of the four individual losses:

$$\mathcal{L}^{total} = \sum_m \mu_m \mathcal{L}_m, \quad (8)$$

with

$$\mu_m = \frac{1}{X_m}, \quad (9)$$

where \mathcal{L}_m is the loss for output m , μ_m is the loss weight for loss m (either the IDH, 1p/19q, grade or segmentation loss), and X_m is the number of samples with known ground truth for output m . In this way, we could counteract the effect of certain outputs having more known labels than other outputs.

F Parameter tuning

Table 8: Hyperparameters that were tuned, and the values that were tested. Values in bold show the selected values used in the final model.

Tuning parameter	Tested values
Dropout rate	0.15, 0.2, 0.25 , 0.30, 0.35, 0.40
l_2 -norm	0.0001, 0.00001 , 0.000001
Learning rate	0.01, 0.001, 0.0001, 0.00001 , 0.0000001
Weight decay	0.001, 0.0001, 0.00001
Augmentation factor	1, 2 , 3
Augmentation probability	0.25, 0.30, 0.35 , 0.40, 0.45

G Evaluation metrics

We calculated the AUC, accuracy, sensitivity, and specificity metrics for the genetic and histological features; for the definitions of these metrics see [67].

For the IDH and 1p/19q co-deletion outputs, the IDH mutated and the 1p/19q co-deleted samples were regarded as the positive class respectively. Since the grade was a multi-class problem, no single positive class could be determined. For the prediction of the individual grades, that grade was seen as the positive class and all other grades as the negative class (e.g., in the case of the grade III prediction, grade III was regarded as the positive class, and grade II and IV were regarded as the negative class). For the LGG vs. HGG prediction, LGG was considered as the positive class and HGG as the negative class. For the evaluation of these metrics for the genetic and histological features, only the subjects with known ground truth were taken into account.

The overall AUC for the grade was a multi-class AUC determined in a one-vs-one approach, comparing each class against the others; in this way, this metric was insensitive to class imbalance [68]. A multi-class accuracy was used to determine the overall accuracy for the grade predictions [67].

To evaluate the performance of the automated segmentation, we evaluated the DICE score, the Hausdorff distance and the volumetric similarity coefficient. The DICE score is a measure of overlap between two segmentations, where a value of 1 indicates perfect overlap, and the Hausdorff distance is a measure of the closeness of the borders of the segmentations. The volumetric similarity coefficient is a measure of the agreement between the volumes of two segmentations, without taking account the actual location of the tumor, where a value of 1 indicates perfect agreement. See [65] for the definitions of these metrics.

H Ground truth labels of patients included from public datasets

[Supplementary file](#)

Acknowledgments

Sebastian van der Voort and Fatih Incekara acknowledge funding by the Dutch Cancer Society (KWF project number EMCR 2015-7859).

Data used in this publication were generated by the National Cancer Institute Clinical Proteomic Tumor Analysis Consortium (CPTAC).

The results published here are in whole or part based upon data generated by the TCGA Research Network: <http://cancergenome.nih.gov/>.

Author contributions

S.R.v.d.V., F.I., W.J.N., M.S., and S.K. contrived the study and designed the experiments. F.I., M.M.J.W., J.W.S., R.N.T., G.J.L., P.C.D.W.H., R.S.E., A.J.P.E.V., M.J.v.d.B., and M.S. included patients in the different studies. S.R.v.d.V., F.I., M.M.J.W., G.K., R.G., J.W.S., R.N.T., G.J.L., P.C.D.W.H., R.S.E., P.J.F., H.J.D., A.J.P.E.V., M.J.v.d.B., and M.S. collected the data. S.R.v.d.V. carried out the experiments. S.R.v.d.V., F.I., M.S., and S.K. interpreted the results. S.R.v.d.V., F.I., M.J.v.d.B., M.S., and S.K. created the initial draft of the paper. M.M.J.W., G.K., R.G., J.W.S., R.N.T., G.J.L., P.C.D.W.H., R.S.E., P.J.F., H.J.D., A.J.P.E.V., W.J.N., and M.J.v.d.B. revised the paper.

References

- [1] OFFICE FOR NATIONAL STATISTICS. *CANCER SURVIVAL IN ENGLAND: Adult, Stage at Diagnosis and Childhood-Patients Followed Up... to 2018*. DANDY BOOKSELLERS Limited, 2019.
- [2] Hendrikus J Dubbink, Peggy N Atmodimedjo, Johan M Kros, Pim J French, Marc Sanson, Ahmed Idbaih, Pieter Wesseling, Roelien Enting, Wim Spliet, Cees Tijssen, Winand N M Dinjens, Thierry Gorlia, and Martin J van den Bent. Molecular classification of anaplastic oligodendroglioma using next-generation sequencing: a report of the prospective randomized EORTC brain tumor group 26951 phase III trial. *Neuro-Oncology*, 18(3):388–400, March 2016. ISSN 1522-8517. URL <https://doi.org/10.1093/neuonc/nov182>.
- [3] Jeanette E Eckel-Passow, Daniel H Lachance, Annette M Molinaro, Kyle M Walsh, Paul A Decker, Hugues Sicotte, Melike Pekmezci, Terri Rice, Matt L Kosel, Ivan V Smirnov, Gobinda Sarkar, Alissa A Caron, Thomas M

- Kollmeyer, Corinne E Praska, Anisha R Chada, Chandralekha Halder, Helen M Hansen, Lucie S McCoy, Paige M Bracci, Roxanne Marshall, Shichun Zheng, Gerald F Reis, Alexander R Pico, Brian P O'Neill, Jan C Buckner, Caterina Giannini, Jason T Huse, Arie Perry, Tarik Tihan, Mitchell S Berger, Susan M Chang, Michael D Prados, Joseph Wiemels, John K Wiencke, Margaret R Wrensch, and Robert B Jenkins. Glioma groups based on 1p/19q, IDH, and TERT promoter mutations in tumors. *New England Journal of Medicine*, 372(26):2499–2508, June 2015. ISSN 0028-4793. URL <https://doi.org/10.1056/NEJMoa1407279>.
- [4] David N Louis, Arie Perry, Guido Reifenberger, Andreas von Deimling, Dominique Figarella-Branger, Webster K Cavenee, Hiroko Ohgaki, Otmar D Wiestler, Paul Kleihues, and David W Ellison. The 2016 world health organization classification of tumors of the central nervous system: a summary. *Acta Neuropathologica*, 131(6):803–820, June 2016. ISSN 0001-6322. URL <https://doi.org/10.1007/s00401-016-1545-1>.
- [5] Ching-Chang Chen, Peng-Wei Hsu, Tai-Wei Erich Wu, Shih-Tseng Lee, Chen-Nen Chang, Kuo-chen Wei, Chih-Cheng Chuang, Chieh-Tsai Wu, Tai-Ngar Lui, Yung-Hsin Hsu, Tzu-Kang Lin, Sai-Cheung Lee, and Yin-Cheng Huang. Stereotactic brain biopsy: Single center retrospective analysis of complications. *Clinical Neurology and Neurosurgery*, 111(10):835–839, December 2009. ISSN 0303-8467. URL <https://doi.org/10.1016/j.clineuro.2009.08.013>.
- [6] Robert J Jackson, Gregory N Fuller, Dima Abi-Said, Frederick F Lang, Ziya L Gokaslan, Wei Ming Shi, David M Wildrick, and Raymond Sawaya. Limitations of stereotactic biopsy in the initial management of gliomas. *Neuro-Oncology*, 3(3):193–200, July 2001. ISSN 1522-8517. URL <https://doi.org/10.1093/neuonc/3.3.193>.
- [7] M Zhou, J Scott, B Chaudhury, L Hall, D Goldgof, KW Yeom, M Iv, Y Ou, J Kalpathy-Cramer, S Napel, R Gillies, O Gevaert, and R Gatenby. Radiomics in brain tumor: Image assessment, quantitative feature descriptors, and machine-learning approaches. *American Journal of Neuroradiology*, 39(2):208–216, February 2018. ISSN 0195-6108. URL <https://doi.org/10.3174/ajnr.A5391>.
- [8] Wenya Linda Bi, Ahmed Hosny, Matthew B Schabath, Maryellen L Giger, Nicolai J Birkbak, Alireza Mehrtash, Tavis Allison, Omar Arnaout, Christopher Abbosh, Ian F Dunn, Raymond H Mak, Rulla M Tamimi, Clare M Tempny, Charles Swanton, Udo Hoffmann, Lawrence H Schwartz, Robert J Gillies, Raymond Y Huang, and Hugo J W L Aerts. Artificial intelligence in cancer imaging: Clinical challenges and applications. *CA: A Cancer Journal for Clinicians*, 69(2):caac.21552, February 2019. ISSN 0007-9235. URL <https://doi.org/10.3322/caac.21552>.

- [9] Ahmad Chaddad, Michael Jonathan Kucharczyk, Paul Daniel, Siham Sabri, Bertrand J Jean-Claude, Tamim Niazi, and Bassam Abdulkarim. Radiomics in glioblastoma: Current status and challenges facing clinical implementation. *Frontiers in Oncology*, 9:374–374, May 2019. ISSN 2234-943X. URL <https://doi.org/10.3389/fonc.2019.00374>.
- [10] Marion Smits. Imaging of oligodendroglioma. *The British Journal of Radiology*, 89(1060):20150857, April 2016. ISSN 0007-1285. URL <https://doi.org/10.1259/bjr.20150857>.
- [11] Rachel L Delfanti, David E Piccioni, Jason Handwerker, Naeim Bahrami, AnithaPriya Krishnan, Roshan Karunamuni, Jona A Hattangadi-Gluth, Tyler M Seibert, Ashwin Srikant, Karra A Jones, Vivian S Snyder, Anders M Dale, Nathan S White, Carrie R McDonald, and Nikdokht Farid. Imaging correlates for the 2016 update on WHO classification of grade II/III gliomas: implications for IDH, 1p/19q and ATRX status. *Journal of Neuro-Oncology*, 135(3):601–609, December 2017. ISSN 0167-594X. URL <https://doi.org/10.1007/s11060-017-2613-7>.
- [12] Sonal Gore, Tanay Chougule, Jayant Jagtap, Jitender Saini, and Madhura Ingahalikar. A review of radiomics and deep predictive modeling in glioma characterization. *Academic Radiology*, July 2020. ISSN 1076-6332. URL <https://doi.org/10.1016/j.acra.2020.06.016>.
- [13] Hugo J W L Aerts, Emmanuel Rios Velazquez, Ralph T H Leijenaar, Chintan Parmar, Patrick Grossmann, Sara Carvalho, Johan Bussink, René Monshouwer, Benjamin Haibe-Kains, Derek Rietveld, Frank Hoebbers, Michelle M Rietbergen, C René Leemans, Andre Dekker, John Quackenbush, Robert J Gillies, and Philippe Lambin. Decoding tumour phenotype by noninvasive imaging using a quantitative radiomics approach. *Nature Communications*, 5(1):4006, September 2014. ISSN 2041-1723. URL <https://doi.org/10.1038/ncomms5006>.
- [14] Sarah Chihati and Djamel Gaceb. A review of recent progress in deep learning-based methods for MRI brain tumor segmentation. In *2020 11th International Conference on Information and Communication Systems (ICICS)*, pages 149–154. Institute of Electrical and Electronics Engineers (IEEE), April 2020. ISBN 9781728162270. URL <https://doi.org/10.1109/icics49469.2020.239550>.
- [15] Robert J Gillies, Paul E Kinahan, and Hedvig Hricak. Radiomics: Images are more than pictures, they are data. *Radiology*, 278(2):563–577, February 2016. ISSN 0033-8419. URL <https://doi.org/10.1148/radiol.2015151169>.
- [16] James H Thrall, Xiang Li, Quanzheng Li, Cinthia Cruz, Synho Do, Keith Dreyer, and James Brink. Artificial intelligence and machine learning in radiology: Opportunities, challenges, pitfalls, and criteria for success. *Journal*

- of the American College of Radiology, 15(3, Part B):504–508, March 2018. ISSN 1546-1440. URL <https://doi.org/10.1016/j.jacr.2017.12.026>.
- [17] Ahmed Hosny, Chintan Parmar, John Quackenbush, Lawrence H Schwartz, and Hugo J W L Aerts. Artificial intelligence in radiology. *Nature Reviews Cancer*, 18(8):500–510, August 2018. ISSN 1474-175X. URL <https://doi.org/10.1038/s41568-018-0016-5>.
 - [18] Okan Kopuklu, Neslihan Kose, Ahmet Gunduz, and Gerhard Rigoll. Resource efficient 3D convolutional neural networks. In *2019 IEEE/CVF International Conference on Computer Vision Workshop (ICCVW)*. Institute of Electrical and Electronics Engineers (IEEE), October 2019. ISBN 9781728150239. URL <https://doi.org/10.1109/iccvw.2019.00240>.
 - [19] S C Thust, S Heiland, A Falini, H R Jäger, A D Waldman, P C Sundgren, C Godi, V K Katsaros, A Ramos, N Bargallo, M W Vernooij, T Yousry, M Bendszus, and M Smits. Glioma imaging in europe: A survey of 220 centres and recommendations for best clinical practice. *European Radiology*, 28(8):3306–3317, August 2018. ISSN 0938-7994. URL <https://doi.org/10.1007/s00330-018-5314-5>.
 - [20] Christian F Freyschlag, Sandro M Krieg, Johannes Kerschbaumer, Daniel Pinggera, Marie-Therese Forster, Dominik Cordier, Marco Rossi, Gabriele Miceli, Alexandre Roux, Andrés Reyes, Silvio Sarubbo, Anja Smits, Joanna Sierpowska, Pierre A Robe, Geert-Jan Rutten, Thomas Santarius, Tomasz Matys, Marc Zanello, Fabien Almairac, Lydiane Mondot, Asgeir S Jakola, Maria Zetterling, Adrià Rofes, Gord von Campe, Remy Guillevin, Daniele Bagatto, Vincent Lubrano, Marion Rapp, John Goodden, Philip C De Witt Hamer, Johan Pallud, Lorenzo Bello, Claudius Thomé, Hugues Duffau, and Emmanuel Mandonnet. Imaging practice in low-grade gliomas among european specialized centers and proposal for a minimum core of imaging. *Journal of Neuro-Oncology*, 139(3):699–711, September 2018. ISSN 0167-594X. URL <https://doi.org/10.1007/s11060-018-2916-3>.
 - [21] M Labussiere, A Idbaih, X-W Wang, Y Marie, B Boisselier, C Falet, S Paris, J Laffaire, C Carpentier, E Criniere, F Ducray, S El Hallani, K Mokhtari, K Hoang-Xuan, J-Y Delattre, and M Sanson. All the 1p19q codeleted gliomas are mutated on IDH1 or IDH2. *Neurology*, 74(23):1886–1890, June 2010. ISSN 0028-3878. URL <https://doi.org/10.1212/WNL.0b013e3181e1cf3a>.
 - [22] David N Louis, Pieter Wesseling, Kenneth Aldape, Daniel J Brat, David Capper, Ian A Cree, Charles Eberhart, Dominique Figarella-Branger, Maryam Fouladi, Gregory N Fuller, Caterina Giannini, Christine Haberler, Cynthia Hawkins, Takashi Komori, Johan M Kros, HK Ng, Brent A Orr, Sung-Hye Park, Werner Paulus, Arie Perry, Torsten Pietsch, Guido Reifenberger, Marc Rosenblum, Brian Rous, Felix Sahm, Chitra Sarkar, David A Solomon, Uri Tabori, Martin J Bent, Andreas Deimling, Michael

- Weller, Valerie A White, and David W Ellison. cIMPACT-NOW update 6: new entity and diagnostic principle recommendations of the cIMPACT-Utrecht meeting on future CNS tumor classification and grading. *Brain Pathology*, 30(4):844–856, July 2020. ISSN 1015-6305. URL <https://doi.org/10.1111/bpa.12832>.
- [23] Zhenyu Tang, Yuyun Xu, Zhicheng Jiao, Junfeng Lu, Lei Jin, Abudumijiti Aibaidula, Jinsong Wu, Qian Wang, Han Zhang, and Dinggang Shen. Pre-operative overall survival time prediction for glioblastoma patients using deep learning on both imaging phenotype and genotype. In Dinggang Shen, Tianming Liu, Terry M Peters, Lawrence H Staib, Caroline Essert, Sean Zhou, Pew-Thian Yap, and Ali Khan, editors, *Lecture Notes in Computer Science*, pages 415–422. Springer Science and Business Media LLC, 2019. ISBN 9783030322380. URL https://doi.org/10.1007/978-3-030-32239-7_46.
- [24] Zhiyuan Xue, Bowen Xin, Dingqian Wang, and Xiuying Wang. Radiomics-enhanced multi-task neural network for non-invasive glioma subtyping and segmentation. In Hassan Mohy-ud Din and Saima Rathore, editors, *Radiomics and Radiogenomics in Neuro-oncology*, pages 81–90. Springer Science and Business Media LLC, 2020. ISBN 9783030401238. URL https://doi.org/10.1007/978-3-030-40124-5_9.
- [25] Milan Decuyper, Stijn Bonte, Karel Deblaere, and Roel Van Hohen. Automated MRI based pipeline for glioma segmentation and prediction of grade, IDH mutation and 1p19q co-deletion, 2020. Preprint at <https://arxiv.org/abs/2005.11965>.
- [26] Stefania Rizzo, Francesca Botta, Sara Raimondi, Daniela Origgi, Cristiana Fanciullo, Alessio Giuseppe Morganti, and Massimo Bellomi. Radiomics: the facts and the challenges of image analysis. *European Radiology Experimental*, 2(1):36, December 2018. ISSN 2509-9280. URL <https://doi.org/10.1186/s41747-018-0068-z>.
- [27] Philipp Lohmann, Norbert Galldiks, Martin Kocher, Alexander Heinzl, Christian P Filss, Carina Stegmayr, Felix M Mottaghy, Gereon R Fink, N Jon Shah, and Karl-Josef Langen. Radiomics in neuro-oncology: Basics, workflow, and applications. *Methods*, June 2020. ISSN 1046-2023. URL <https://doi.org/10.1016/j.ymeth.2020.06.003>.
- [28] Stephen S F Yip and Hugo J W L Aerts. Applications and limitations of radiomics. *Physics in Medicine and Biology*, 61(13):R150–R166, July 2016. ISSN 0031-9155. URL <https://doi.org/10.1088/0031-9155/61/13/r150>.
- [29] Annika Malmström, Małgorzata Lysiak, Bjarne Winther Kristensen, Elizabeth Hovey, Roger Henriksson, and Peter Söderkvist. Do we really know who has an MGMT methylated glioma? Results of an international survey

- regarding use of MGMT analyses for glioma. *Neuro-Oncology Practice*, 7 (1):68–76, 09 2019. ISSN 2054-2577. URL <https://doi.org/10.1093/nop/npz039>.
- [30] Takahiro Sasaki, Manabu Kinoshita, Koji Fujita, Junya Fukai, Nobuhide Hayashi, Yuji Uematsu, Yoshiko Okita, Masahiro Nonaka, Shusuke Moriuchi, Takehiro Uda, Naohiro Tsuyuguchi, Hideyuki Arita, Kanji Mori, Kenichi Ishibashi, Koji Takano, Namiko Nishida, Tomoko Shofuda, Ema Yoshioka, Daisuke Kanematsu, Yoshinori Kodama, Masayuki Mano, Naoyuki Nakao, and Yonehiro Kanemura. Radiomics and MGMT promoter methylation for prognostication of newly diagnosed glioblastoma. *Scientific Reports*, 9(1):14435, December 2019. ISSN 2045-2322. URL <https://doi.org/10.1038/s41598-019-50849-y>.
 - [31] A Gupta, A Prager, RJ Young, W Shi, AMP Omuro, and JJ Graber. Diffusion-weighted MR imaging and MGMT methylation status in glioblastoma: A reappraisal of the role of preoperative quantitative ADC measurements. *American Journal of Neuroradiology*, 34(1):E10–E11, January 2013. ISSN 0195-6108. URL <https://doi.org/10.3174/ajnr.A3467>.
 - [32] JA Carrillo, A Lai, PL Nghiemphu, HJ Kim, HS Phillips, S Kharbanda, P Moftakhar, S Lalaezari, W Yong, BM Ellingson, TF Cloughesy, and WB Pope. Relationship between tumor enhancement, edema, IDH1 mutational status, MGMT promoter methylation, and survival in glioblastoma. *American Journal of Neuroradiology*, 33(7):1349–1355, August 2012. ISSN 0195-6108. URL <https://doi.org/10.3174/ajnr.A2950>.
 - [33] Vilde Elisabeth Mikkelsen, Hong Yan Dai, Anne Line Stensjøen, Erik Magnus Berntsen, Øyvind Salvesen, Ole Solheim, and Sverre Helge Torp. MGMT promoter methylation status is not related to histological or radiological features in IDH wild-type glioblastomas. *Journal of Neuropathology & Experimental Neurology*, 79(8):855–862, August 2020. ISSN 0022-3069. URL <https://doi.org/10.1093/jnen/nlaa060>.
 - [34] Martin J. van den Bent. Interobserver variation of the histopathological diagnosis in clinical trials on glioma: a clinician’s perspective. *Acta Neuropathologica*, 120(3):297–304, September 2010. ISSN 1432-0533. URL <https://doi.org/10.1007/s00401-010-0725-7>.
 - [35] Ji Eun Park, Ho Sung Kim, Youngheun Jo, Roh-Eul Yoo, Seung Hong Choi, Soo Jung Nam, and Jeong Hoon Kim. Radiomics prognostication model in glioblastoma using diffusion- and perfusion-weighted MRI. *Scientific Reports*, 10(1):4250, December 2020. ISSN 2045-2322. URL <https://doi.org/10.1038/s41598-020-61178-w>.
 - [36] Minjae Kim, So Yeong Jung, Ji Eun Park, Yeongheun Jo, Seo Young Park, Soo Jung Nam, Jeong Hoon Kim, and Ho Sung Kim. Diffusion- and perfusion-weighted MRI radiomics model may predict isocitrate dehydrogenase (IDH) mutation and tumor aggressiveness in diffuse lower grade

- glioma. *European Radiology*, 30(4):2142–2151, April 2020. ISSN 0938-7994. URL <https://doi.org/10.1007/s00330-019-06548-3>.
- [37] M Visser, DMJ Müller, RJM van Duijn, M Smits, N Verburg, EJ Hendriks, RJA Nabuurs, JCJ Bot, RS Eijgelaar, M Witte, MB van Herk, F Barkhof, PC de WittHammer, and JC de Munck. Inter-rater agreement in glioma segmentations on longitudinal MRI. *NeuroImage: Clinical*, 22:101727, 2019. ISSN 2213-1582. URL <https://doi.org/10.1016/j.nicl.2019.101727>.
 - [38] Kenneth Clark, Bruce Vendt, Kirk Smith, John Freymann, Justin Kirby, Paul Koppel, Stephen Moore, Stanley Phillips, David Maffitt, Michael Pringle, Lawrence Tarbox, and Fred Prior. The cancer imaging archive (TCIA): Maintaining and operating a public information repository. *Journal of Digital Imaging*, 26(6):1045–1057, December 2013. ISSN 0897-1889. URL <https://doi.org/10.1007/s10278-013-9622-7>.
 - [39] Lisa Scarpance, Adam E Flanders, Rajan Jain, Tom Mikkelsen, and David W Andrews. Data from REMBRANDT. The Cancer Imaging Archive, 2015. URL <https://doi.org/10.7937/K9/TCIA.2015.5880ZUZB>.
 - [40] National Cancer Institute Clinical Proteomic Tumor Analysis Consortium (CPTAC). Radiology data from the clinical proteomic tumor analysis consortium glioblastoma multiforme CPTAC-GBM collection. The Cancer Imaging Archive, 2018. URL <https://doi.org/10.7937/k9/tcia.2018.3rje41q1>.
 - [41] Nameeta Shah, Xu Feng, Michael Lankerovich, Ralph B Puchalski, and Bart Keogh. Data from Ivy GAP. The Cancer Imaging Archive, 2016. URL <https://doi.org/10.7937/K9/TCIA.2016.XLwaN6nL>.
 - [42] Ralph B Puchalski, Nameeta Shah, Jeremy Miller, Rachel Dalley, Steve R Nomura, Jae-Guen Yoon, Kimberly A Smith, Michael Lankerovich, Darren Bertagnolli, Kris Bickley, Andrew F Boe, Krissy Brouner, Stephanie Butler, Shiella Caldejon, Mike Chapin, Suvro Datta, Nick Dee, Tsega Desta, Tim Dolbeare, Nadezhda Dotson, Amanda Ebbert, David Feng, Xu Feng, Michael Fisher, Garrett Gee, Jeff Goldy, Lindsey Gourley, Benjamin W Gregor, Guangyu Gu, Nika Hejazi, John Hohmann, Parvinder Hothi, Robert Howard, Kevin Joines, Ali Kriedberg, Leonard Kuan, Chris Lau, Felix Lee, Hwahyung Lee, Tracy Lemon, Fuhui Long, Naveed Mastan, Erika Mott, Chantal Murthy, Kiet Ngo, Eric Olson, Melissa Reding, Zack Riley, David Rosen, David Sandman, Nadiya Shapovalova, Clifford R Slaughterbeck, Andrew Sodt, Graham Stockdale, Aaron Szafer, Wayne Wakeman, Paul E Wohnoutka, Steven J White, Don Marsh, Robert C Rostomily, Lydia Ng, Chinh Dang, Allan Jones, Bart Keogh, Haley R Gittleman, Jill S Barnholtz-Sloan, Patrick J Cimino, Megha S Uppin, C Dirk Keene, Farrokh R Farrokhi, Justin D Lathia, Michael E Berens, Antonio Iavarone, Amy Bernard, Ed Lein, John W Phillips, Steven W Rostad, Charles Cobbs,

- Michael J Hawrylycz, and Greg D Foltz. An anatomic transcriptional atlas of human glioblastoma. *Science*, 360(6389):660–663, May 2018. ISSN 0036-8075. URL <https://doi.org/10.1126/science.aaf2666>.
- [43] Kathleen Schmainda and Melissa Prah. Data from Brain-Tumor-Progression. The Cancer Imaging Archive, 2018. URL <https://doi.org/10.7937/K9/TCIA.2018.15quzvnv>.
- [44] B. H. Menze, A. Jakab, S. Bauer, J. Kalpathy-Cramer, K. Farahani, J. Kirby, Y. Burren, N. Porz, J. Slotboom, R. Wiest, L. Lanczi, E. Gerstner, M. Weber, T. Arbel, B. B. Avants, N. Ayache, P. Buendia, D. L. Collins, N. Cordier, J. J. Corso, A. Criminisi, T. Das, H. Delingette, Ç. Demiralp, C. R. Durst, M. Dojat, S. Doyle, J. Festa, F. Forbes, E. Geremia, B. Glocker, P. Golland, X. Guo, A. Hamamci, K. M. Iftekharuddin, R. Jena, N. M. John, E. Konukoglu, D. Lashkari, J. A. Mariz, R. Meier, S. Pereira, D. Precup, S. J. Price, T. R. Raviv, S. M. S. Reza, M. Ryan, D. Sarikaya, L. Schwartz, H. Shin, J. Shotton, C. A. Silva, N. Sousa, N. K. Subbanna, G. Szekely, T. J. Taylor, O. M. Thomas, N. J. Tustison, G. Unal, F. Vasseur, M. Wintermark, D. H. Ye, L. Zhao, B. Zhao, D. Zikic, M. Prastawa, M. Reyes, and K. Van Leemput. The multimodal brain tumor image segmentation benchmark (BRATS). *IEEE Transactions on Medical Imaging*, 34(10):1993–2024, 2015. URL <https://doi.org/10.1109/TMI.2014.2377694>.
- [45] Spyridon Bakas, Hamed Akbari, Aristeidis Sotiras, Michel Bilello, Martin Rozycki, Justin S Kirby, John B Freymann, Keyvan Farahani, and Christos Davatzikos. Advancing the cancer genome atlas glioma MRI collections with expert segmentation labels and radiomic features. *Scientific Data*, 4(1):170117, December 2017. ISSN 2052-4463. URL <https://doi.org/10.1038/sdata.2017.117>.
- [46] Spyridon Bakas, Mauricio Reyes, Andras Jakab, Stefan Bauer, Markus Rempfler, Alessandro Crimi, Russell Takeshi Shinohara, Christoph Berger, Sung Min Ha, Martin Rozycki, Marcel Prastawa, Esther Alberts, Jana Lipkova, John Freymann, Justin Kirby, Michel Bilello, Hassan Fathallah-Shaykh, Roland Wiest, Jan Kirschke, Benedikt Wiestler, Rivka Colen, Aikaterini Kotrotsou, Pamela Lamontagne, Daniel Marcus, Mikhail Milchenko, Arash Nazeri, Marc-Andre Weber, Abhishek Mahajan, Ujjwal Baid, Elizabeth Gerstner, Dongjin Kwon, Gagan Acharya, Manu Agarwal, Mahbubul Alam, Alberto Albiol, Antonio Albiol, Francisco J. Albiol, Varghese Alex, Nigel Allinson, Pedro H. A. Amorim, Abhijit Amrutkar, Ganesh Anand, Simon Andermatt, Tal Arbel, Pablo Arbelaez, Aaron Avery, Muneeza Azmat, Pranjal B., W Bai, Subhashis Banerjee, Bill Barth, Thomas Batchelder, Kayhan Batmanghelich, Enzo Battistella, Andrew Beers, Mikhail Belyaev, Martin Bendszus, Eze Benson, Jose Bernal, Halandur Nagaraja Bharath, George Biros, Sotirios Bisdas, James Brown, Mariano Cabezas, Shilei Cao, Jorge M. Cardoso, Eric N Carver, Adria

Casamitjana, Laura Silvana Castillo, Marcel Catà, Philippe Cattin, Albert Cerigues, Vinicius S. Chagas, Siddhartha Chandra, Yi-Ju Chang, Shiyu Chang, Ken Chang, Joseph Chazalon, Shengcong Chen, Wei Chen, Jefferson W Chen, Zhaolin Chen, Kun Cheng, Ahana Roy Choudhury, Roger Chylla, Albert Clérigues, Steven Coleman, Ramiro German Rodriguez Colmeiro, Marc Combalia, Anthony Costa, Xiaomeng Cui, Zhenzhen Dai, Lutao Dai, Laura Alexandra Daza, Eric Deutsch, Changxing Ding, Chao Dong, Shidu Dong, Wojciech Dudzik, Zach Eaton-Rosen, Gary Egan, Guilherme Escudero, Théo Estienne, Richard Everson, Jonathan Fabrizio, Yong Fan, Longwei Fang, Xue Feng, Enzo Ferrante, Lucas Fidon, Martin Fischer, Andrew P. French, Naomi Fridman, Huan Fu, David Fuentes, Yaozong Gao, Evan Gates, David Gering, Amir Gholami, Willi Gierke, Ben Glocker, Mingming Gong, Sandra González-Villá, T. Gros-ges, Yuanfang Guan, Sheng Guo, Sudeep Gupta, Woo-Sup Han, Il Song Han, Konstantin Harmuth, Huiguang He, Aura Hernández-Sabaté, Evelyn Herrmann, Naveen Himthani, Winston Hsu, Cheyu Hsu, Xiaojun Hu, Xiaobin Hu, Yan Hu, Yifan Hu, Rui Hua, Teng-Yi Huang, Weilin Huang, Sabine Van Huffel, Quan Huo, Vivek HV, Khan M. Iftekharruddin, Fabian Isensee, Mobarakol Islam, Aaron S. Jackson, Sachin R. Jambawalikar, Andrew Jesson, Weijian Jian, Peter Jin, V Jeya Maria Jose, Alain Jungo, B Kainz, Konstantinos Kamnitsas, Po-Yu Kao, Ayush Karnawat, Thomas Kellermeyer, Adel Kermi, Kurt Keutzer, Mohamed Tarek Khadir, Mahendra Khened, Philipp Kickingeder, Geena Kim, Nik King, Haley Knapp, Urs peter Knecht, Lisa Kohli, Deren Kong, Xiangmao Kong, Simon Koppers, Avinash Kori, Ganapathy Krishnamurthi, Egor Krivov, Piyush Kumar, Kaisar Kushibar, Dmitrii Lachinov, Tryphon Lambrou, Joon Lee, Chengen Lee, Yuehchou Lee, M Lee, Szidonia Lefkovits, Laszlo Lefkovits, James Levitt, Tengfei Li, Hongwei Li, Wenqi Li, Hongyang Li, Xiaochuan Li, Yuexiang Li, Heng Li, Zhenye Li, Xiaoyu Li, Zeju Li, XiaoGang Li, Wenqi Li, Zheng-Shen Lin, Fengming Lin, Pietro Lio, Chang Liu, Boqiang Liu, Xiang Liu, Mingyuan Liu, Ju Liu, Luyan Liu, Xavier Llado, Marc Moreno Lopez, Pablo Ribalta Lorenzo, Zhentai Lu, Lin Luo, Zhigang Luo, Jun Ma, Kai Ma, Thomas Mackie, Anant Madabushi, Issam Mahmoudi, Klaus H. Maier-Hein, Pradipta Maji, CP Mammen, Andreas Mang, B. S. Manjunath, Michal Marcinkiewicz, S McDonagh, Stephen McKenna, Richard McKinley, Miriam Mehl, Sachin Mehta, Raghav Mehta, Raphael Meier, Christoph Meinel, Dorit Merhof, Craig Meyer, Robert Miller, Sushmita Mitra, Aliasgar Moiyadi, David Molina-Garcia, Miguel A. B. Monteiro, Grzegorz Mrukwa, Andriy Myronenko, Jakub Nalepa, Thuyen Ngo, Dong Nie, Holly Ning, Chen Niu, Nicholas K Nuechterlein, Eric Oermann, Arlindo Oliveira, Diego D. C. Oliveira, Arnau Oliver, Alexander F. I. Osman, Yu-Nian Ou, Sebastien Ourselin, Nikos Paragios, Moo Sung Park, Brad Paschke, J. Gregory Pauloski, Kamlesh Pawar, Nick Pawlowski, Linmin Pei, Suting Peng, Silvio M. Pereira, Julian Perez-Beteta, Victor M. Perez-Garcia, Simon Pezold, Bao Pham, Ashish Phophalia, Gemma Piella, G. N. Pillai, Marie Piraud, Maxim Pisov, Anmol Popli, Michael P.

Pound, Reza Pourreza, Prateek Prasanna, Vesna Prkovska, Tony P. Pridmore, Santi Puch, Élodie Puybureau, Buyue Qian, Xu Qiao, Martin Rajchl, Swapnil Rane, Michael Rebsamen, Hongliang Ren, Xuhua Ren, Karthik Revanuru, Mina Rezaei, Oliver Rippel, Luis Carlos Rivera, Charlotte Robert, Bruce Rosen, Daniel Rueckert, Mohammed Safwan, Mostafa Salem, Joaquim Salvi, Irina Sanchez, Irina Sánchez, Heitor M. Santos, Emmett Sartor, Dawid Schellingerhout, Klaudius Scheufele, Matthew R. Scott, Artur A. Scussel, Sara Sedlar, Juan Pablo Serrano-Rubio, N. Jon Shah, Nameetha Shah, Mazhar Shaikh, B. Uma Shankar, Zeina Shboul, Haipeng Shen, Dinggang Shen, Linlin Shen, Haocheng Shen, Varun Shenoy, Feng Shi, Hyung Eun Shin, Hai Shu, Diana Sima, M Sinclair, Orjan Smedby, James M. Snyder, Mohammadreza Soltaninejad, Guidong Song, Mehul Soni, Jean Stawiaski, Shashank Subramanian, Li Sun, Roger Sun, Jiawei Sun, Kay Sun, Yu Sun, Guoxia Sun, Shuang Sun, Yannick R Suter, Laszlo Szilagyi, Sanjay Talbar, Dacheng Tao, Dacheng Tao, Zhongzhao Teng, Siddhesh Thakur, Meenakshi H Thakur, Sameer Tharakan, Pallavi Tiwari, Guillaume Tochon, Tuan Tran, Yuhsiang M. Tsai, Kuan-Lun Tseng, Tran Anh Tuan, Vadim Turlapov, Nicholas Tustison, Maria Vakalopoulou, Sergi Valverde, Rami Vanguri, Evgeny Vasiliev, Jonathan Ventura, Luis Vera, Tom Vercauteren, C. A. Verrastro, Lasitha Vidyaratne, Veronica Vilaplana, Ajeet Vivekanandan, Guotai Wang, Qian Wang, Chiatse J. Wang, Weichung Wang, Duo Wang, Ruixuan Wang, Yuanyuan Wang, Chunliang Wang, Guotai Wang, Ning Wen, Xin Wen, Leon Weninger, Wolfgang Wick, Shaocheng Wu, Qiang Wu, Yihong Wu, Yong Xia, Yanwu Xu, Xiaowen Xu, Peiyuan Xu, Tsai-Ling Yang, Xiaoping Yang, Hao-Yu Yang, Junlin Yang, Haojin Yang, Guang Yang, Hongdou Yao, Xujiang Ye, Changchang Yin, Brett Young-Moxon, Jinhua Yu, Xiangyu Yue, Songtao Zhang, Angela Zhang, Kun Zhang, Xuejie Zhang, Lichi Zhang, Xiaoyue Zhang, Yazhuo Zhang, Lei Zhang, Jianguo Zhang, Xiang Zhang, Tianhao Zhang, Sicheng Zhao, Yu Zhao, Xiaomei Zhao, Liang Zhao, Yefeng Zheng, Liming Zhong, Chenhong Zhou, Xiaobing Zhou, Fan Zhou, Hongtu Zhu, Jin Zhu, Ying Zhuge, Weiwei Zong, Jayashree Kalpathy-Cramer, Keyvan Farahani, Christos Davatzikos, Koen van Leemput, and Bjoern Menze. Identifying the best machine learning algorithms for brain tumor segmentation, progression assessment, and overall survival prediction in the BRATS challenge, 2018. Preprint at <https://arxiv.org/abs/1811.02629>.

- [47] Nancy Pedano, Adam E Flanders, Lisa Scarpance, Tom Mikkelsen, Jennifer M Eschbacher, Beth Hermes, Victor Sisneros, Jill Barnholtz-Sloan, and Quinn Ostrom. Radiology data from the cancer genome atlas low grade glioma [TCGA-LGG] collection. The Cancer Imaging Archive, 2016. URL <https://doi.org/10.7937/K9/TCIA.2016.L4LTD3TK>.
- [48] Lisa Scarpance, Tom Mikkelsen, Soonmee Cha, Sujaya Rao, Sangeeta Tekchandani, David Gutman, Joel H Saltz, Bradley J Erickson, Nancy Pedano, Adam E Flanders, Jill Barnholtz-Sloan, Quinn Ostrom, Daniel Barboriak, and Laura J Pierce. Radiology data from the cancer genome

- atlas glioblastoma multiforme [TCGA-GBM] collection. The Cancer Imaging Archive, 2016. URL <https://doi.org/10.7937/K9/TCIA.2016.RNYFUYE9>.
- [49] Spyridon Bakas, Hamed Akbari, Aristeidis Sotiras, Michel Bilello, Martin Rozycki, Justin Kirby, John Freymann, Keyvan Farahani, and Christos Davatzikos. Segmentation labels and radiomic features for the pre-operative scans of the TCGA-LGG collection [data set] The Cancer Imaging Archive, 2017. URL <https://doi.org/10.7937/K9/TCIA.2017.GJQ7R0EF>.
 - [50] Spyridon Bakas, Hamed Akbari, Aristeidis Sotiras, Michel Bilello, Martin Rozycki, Justin Kirby, John Freymann, Keyvan Farahani, and Christos Davatzikos. Segmentation labels and radiomic features for the pre-operative scans of the TCGA-GBM collection [data set]. The Cancer Imaging Archive, 2017. URL <https://doi.org/10.7937/K9/TCIA.2017.KLXWJJ1Q>.
 - [51] Xiangrui Li, Paul S Morgan, John Ashburner, Jolinda Smith, and Christopher Rorden. The first step for neuroimaging data analysis: DICOM to NIFTI conversion. *Journal of Neuroscience Methods*, 264:47–56, May 2016. ISSN 0165-0270. URL <https://doi.org/10.1016/j.jneumeth.2016.03.001>.
 - [52] Vladimir Fonov, Alan C Evans, Kelly Botteron, C Robert Almli, Robert C McKinsty, and D Louis Collins. Unbiased average age-appropriate atlases for pediatric studies. *NeuroImage*, 54(1):313–327, January 2011. ISSN 1053-8119. URL <https://doi.org/10.1016/j.neuroimage.2010.07.033>.
 - [53] VS Fonov, AC Evans, RC McKinsty, CR Almli, and DL Collins. Unbiased nonlinear average age-appropriate brain templates from birth to adulthood. *NeuroImage*, 47:S102, July 2009. ISSN 1053-8119. URL [https://doi.org/10.1016/S1053-8119\(09\)70884-5](https://doi.org/10.1016/S1053-8119(09)70884-5). Organization for Human Brain Mapping 2009 Annual Meeting.
 - [54] S Klein, M Staring, K Murphy, MA Viergever, and J Pluim. elastix: A toolbox for intensity-based medical image registration. *IEEE Transactions on Medical Imaging*, 29(1):196–205, January 2010. ISSN 0278-0062. URL <https://doi.org/10.1109/TMI.2009.2035616>.
 - [55] Denis Shamonin. Fast parallel image registration on CPU and GPU for diagnostic classification of alzheimer’s disease. *Frontiers in Neuroinformatics*, 7:50, 2013. ISSN 1662-5196. URL <https://doi.org/10.3389/fninf.2013.00050>.
 - [56] Bradley C Lowekamp, David T Chen, Luis Ibáñez, and Daniel Blezek. The design of SimpleITK. *Frontiers in Neuroinformatics*, 7:45, 2013. ISSN 1662-5196. URL <https://doi.org/10.3389/fninf.2013.00045>.

- [57] Fabian Isensee, Marianne Schell, Irada Pfueger, Gianluca Brugnara, David Bonekamp, Ulf Neuberger, Antje Wick, Heinz-Peter Schlemmer, Sabine Heiland, Wolfgang Wick, Martin Bendszus, Klaus H Maier-Hein, and Philipp Kickingereder. Automated brain extraction of multisequence MRI using artificial neural networks. *Human Brain Mapping*, 40(17):4952–4964, December 2019. ISSN 1065-9471. URL <https://doi.org/10.1002/hbm.24750>.
- [58] Olaf Ronneberger. Invited talk: U-net convolutional networks for biomedical image segmentation. In geb Fritzsche K Maier-Hein, geb Lehmann T Deserno, Heinz Handels, and Thomas Tolxdorff, editors, *Bildverarbeitung für die Medizin 2017. Informatik aktuell*, pages 3–3. Springer Science and Business Media LLC, 2017. ISBN 9783662543443. URL https://doi.org/10.1007/978-3-662-54345-0_3.
- [59] Martín Abadi, Paul Barham, Jianmin Chen, Zhifeng Chen, Andy Davis, Jeffrey Dean, Matthieu Devin, Sanjay Ghemawat, Geoffrey Irving, Michael Isard, Manjunath Kudlur, Josh Levenberg, Rajat Monga, Sherry Moore, Derek G Murray, Benoit Steiner, Paul Tucker, Vijay Vasudevan, Pete Warden, Martin Wicke, Yuan Yu, and Xiaoqiang Zheng. TensorFlow: A system for large-scale machine learning. In *12th USENIX Symposium on Operating Systems Design and Implementation (OSDI 16)*, pages 265–283. USENIX Association, November 2016. ISBN 978-1-931971-33-1. URL <https://www.usenix.org/conference/osdi16/technical-sessions/presentation/abadi>.
- [60] Dipankar Das, Naveen Mellempudi, Dheevatsa Mudigere, Dhiraj Kalamkar, Sasikanth Avancha, Kunal Banerjee, Srinivas Sridharan, Karthik Vaidyanathan, Bharat Kaul, Evangelos Georganas, Alexander Heinecke, Pradeep Dubey, Jesus Corbal, Nikita Shustrov, Roma Dubtsov, Evarist Fomenko, and Vadim Pirogov. Mixed precision training of convolutional neural networks using integer operations. In *International Conference on Learning Representations*, 2018. URL <https://openreview.net/forum?id=H135uzZ0->.
- [61] Samuel L. Smith, Pieter-Jan Kindermans, and Quoc V. Le. Don’t decay the learning rate, increase the batch size. In *International Conference on Learning Representations*, 2018. URL <https://openreview.net/forum?id=B1Yy1BxCZ>.
- [62] Cliff Woolley. NCCL: accelerated multi-GPU collective communications. URL <https://images.nvidia.com/events/sc15/pdfs/NCCL-Woolley.pdf>. Accessed on 2020-09-30.
- [63] Ilya Loshchilov and Frank Hutter. Decoupled weight decay regularization, 2017. Preprint at <https://arxiv.org/abs/1711.05101>.

- [64] F. Pedregosa, G. Varoquaux, A. Gramfort, V. Michel, B. Thirion, O. Grisel, M. Blondel, P. Prettenhofer, R. Weiss, V. Dubourg, J. Vanderplas, A. Passos, D. Cournapeau, M. Brucher, M. Perrot, and E. Duchesnay. Scikit-learn: Machine learning in python. *Journal of Machine Learning Research*, 12:2825–2830, 2011. URL <https://www.jmlr.org/papers/v12/pedregosa11a.html>.
- [65] Abdel Aziz Taha and Allan Hanbury. Metrics for evaluating 3d medical image segmentation: analysis, selection, and tool. *BMC Medical Imaging*, 15(1):29, August 2015. ISSN 1471-2342. URL <https://doi.org/10.1186/s12880-015-0068-x>.
- [66] Daniel Smilkov, Nikhil Thorat, Been Kim, Fernanda Viégas, and Martin Wattenberg. SmoothGrad: removing noise by adding noise, 2017. Preprint at <https://arxiv.org/abs/1706.03825>.
- [67] Alaa Tharwat. Classification assessment methods. *Applied Computing and Informatics*, 2018. ISSN 2210-8327. URL <https://doi.org/10.1016/j.aci.2018.08.003>.
- [68] David J. Hand and Robert J. Till. A simple generalisation of the area under the ROC curve for multiple class classification problems. *Machine Learning*, 45(2):171–186, November 2001. ISSN 1573-0565. URL <https://doi.org/10.1023/A:1010920819831>.